

# A Perturbation-Correction Method Based on Local Randomized Neural Networks for Quasi-Linear Interface Problems

Siyuan Lang<sup>a</sup>, Zhiyue Zhang<sup>a,\*</sup>

<sup>a</sup>*Ministry of Education Key Laboratory for NSLSCS, School of Mathematical Sciences, Nanjing Normal University, Nanjing, China*

---

## Abstract

For quasi-linear interface problems with discontinuous diffusion coefficients, the nonconvex objective functional often leads to optimization stagnation in randomized neural network approximations. This paper proposes a perturbation-correction framework based on Local Randomized Neural Networks (LRaNNs) to overcome this limitation. In the initialization step, a satisfactory base approximation is obtained by minimizing the original nonconvex residual, typically stagnating at a moderate accuracy level. Subsequently, in the correction step, a correction term is determined by solving a subproblem governed by a perturbation expansion around the base approximation. This reformulation yields a convex optimization problem for the output coefficients, which guarantees rapid convergence. We rigorously derive an *a posteriori* error estimate, demonstrating that the total generalization error is governed by the discrete residual norm, quadrature error, and a controllable truncation error. Numerical experiments on nonlinear diffusion problems with irregular moving interfaces, gradient-dependent diffusivities, and high-contrast media demonstrate that the proposed method effectively overcomes the optimization plateau. The correction step yields a significant improvement of 4 – 6 orders of magnitude in  $L^2$  accuracy.

**Keywords:** Operator splitting method, Stefan problem, Extreme Learning Machines, Predictor Corrector, Convex optimization

**2020 MSC:** 35R35, 65M12, 65M70, 65K10

---

## 1. Introduction

Interface problems with nonlinear diffusion coefficients [1] arise in a wide range of physical and engineering contexts, including composite material manufacturing [2, 3], battery electrochemistry [4, 5], and biological transport processes [6, 7], where discontinuities across material interfaces are fundamental features. The prevalence of such phenomena underscores the importance of developing accurate and efficient numerical solvers.

Although nonlinear interface problems are of significant practical relevance, much of the numerical analysis has historically focused on their linear counterparts. Classical approaches such as the finite difference method (FDM) [8], the finite volume method (FVM) [9, 10], the immersed interface method (IIM) [11, 12], the matched interface and boundary method (MIB) [13, 14] and the ghost fluid method (GFM) [15, 16] as well as the finite element method (FEM) [17] have achieved high accuracy by employing interface-conforming meshes. Numerous refinements—such as generalized FEM [18, 19], immersed FEM [20], and cut FEM [21]—have increased flexibility, particularly in handling complicated or dynamic interface geometries. Additional contributions rooted in traditional formulations for linear interface problems can be found in [22, 23, 24, 25, 26, 27], and the references therein. More recently, these mesh-based formulations have

---

\*Corresponding author.

Email address: [zhangzhiyue@njnu.edu.cn](mailto:zhangzhiyue@njnu.edu.cn) (Zhiyue Zhang)

been adapted to nonlinear cases; for example, [28] developed immersed methods on interface-independent meshes for nonlinear (quasi-linear) elliptic problems with discontinuous diffusion.

In parallel, mesh-free techniques have emerged as a powerful alternative for interface problems. Among these, physics-informed neural networks (PINNs) [29], the deep Galerkin method [30], and the deep Ritz method [31] formulate the solution of partial differential equations as unconstrained optimization problems, thus bypassing mesh generation and offering remarkable flexibility for high-dimensional and complex geometries. We also note that multi-stage training strategies have been investigated in the PINNs framework [32, 33], where the solution process for linear PDEs is partitioned into successive nonconvex optimization stages in order to improve convergence. In addition, randomized neural networks (RaNNs) [34] and extreme learning machines (ELMs) [35] have gained prominence for their mesh-free frameworks, where the hidden-layer parameters are randomly generated and fixed, and only the output layer is optimized, typically via convex least-squares solvers. These models are supported by a well-established theory demonstrating their universal approximation capabilities under suitable conditions [36, 37]. Recently, such neural network approaches have been specifically applied to interface problems, where their ability to accommodate discontinuities and capture complex interface effects is particularly advantageous [38, 39, 40, 41, 42, 43, 44, 45, 46, 47, 48, 49, 50, 51, 52, 53]. These neural network frameworks have been successfully applied to nonlinear PDEs, including nonlinear elliptic and parabolic equations, as in [54, 55, 56], motivating its extension to nonlinear interface settings. Moreover, recent works have begun to rigorously analyze the approximation error and generalization properties of mesh-free neural network solvers in the context of PDE problems, e.g., [57, 58]. Nevertheless, highly accurate machine learning-based approaches for nonlinear interface problems remain limited, primarily due to the nonconvexity of the resulting residual minimization. The development of efficient solvers in this context is thus both challenging and significant.

In this work, we propose a perturbation-correction method implemented via Local Randomized Neural Networks (LRaNNs) for the efficient and robust solution of quasi-linear interface problems. In the first step, the original nonconvex PDE residual minimization is solved locally via LRaNNs, producing a convergent base approximation that captures the primary interfacial behavior. Subsequently, in the perturbation-correction step, we apply a perturbation expansion about the first-step numerical solution, thereby reformulating the correction step as a convex optimization problem in the output coefficients. In both steps, the resulting optimization problems are efficiently solved via Gauss-Newton iterations, ensuring rapid convergence and high accuracy. Furthermore, we establish *a posteriori* generalization error bounds for the  $L^2$ -norm of the gradient error  $\nabla e$  in both steps and show that the correction step significantly reduces the optimization error term associated with the residual of the initial-step approximation. Finally, to demonstrate effectiveness and robustness, we present numerical tests on representative problems, including nonlinear diffusion with irregular interfaces, high-contrast media, gradient-dependent coefficients, and time-dependent extensions with moving interfaces.

The main contributions are as follows:

1. A perturbation-correction framework for quasi-linear interface problems, combining Gauss-Newton initialization on LRaNNs with a perturbation-expansion correction step to overcome optimization stagnation in nonconvex residual minimization.
2. A complete *a posteriori* error analysis for both steps, showing that the correction step solves a convex subproblem that effectively eliminates the leading-order initialization error, with explicit bounds derived in terms of residual norms, quadrature error, and perturbation truncation.
3. Numerical experiments over challenging scenarios—including irregular and moving interfaces, large contrasts, and coefficient nonlinearities in both  $u$  and  $\nabla u$ —demonstrate consistent and significant error reduction between the two steps, achieving up to 4–6 orders of magnitude improvement in  $L^2$  accuracy and exhibiting stable performance across all tested cases.

The remainder of this paper is organized as follows. Section 2 introduces the quasi-linear interface model and assumptions. Section 3 describes the LRaNNs formulation and perturbation correction method. Section 4 presents the error analysis and convexity results. Section 5 reports numerical experiments, and Section 6 concludes the paper.

## 2. Problem Formulation

We consider a class of quasi-linear elliptic interface problems involving solution-dependent diffusion coefficients, nonlinear source terms, and prescribed jump conditions across the interface:

$$\begin{cases} -\nabla \cdot (\beta^+(x, u^+) \nabla u^+) = f^+(x, u^+), & x \in \Omega^+, \\ -\nabla \cdot (\beta^-(x, u^-) \nabla u^-) = f^-(x, u^-), & x \in \Omega^-, \\ \llbracket u(x) \rrbracket = w(x), & x \in \Gamma, \\ \llbracket \beta(x, u) \frac{\partial u}{\partial \mathbf{n}} \rrbracket = v(x), & x \in \Gamma, \\ u(x) = g(x), & x \in \partial\Omega. \end{cases} \quad (1)$$

Let  $\Omega \subset \mathbb{R}^d$  be a bounded domain with Lipschitz boundary  $\partial\Omega$ . We assume that  $\Omega$  is decomposed into two non-overlapping subdomains  $\Omega^+$  and  $\Omega^-$  as depicted in Fig. 1, i.e.,

$$\overline{\Omega} = \overline{\Omega^+} \cup \overline{\Omega^-}, \quad \Omega^+ \cap \Omega^- = \emptyset, \quad \Gamma = \partial\Omega^+ \cap \partial\Omega^-,$$

where  $\Gamma$  denotes the interface separating  $\Omega^+$  and  $\Omega^-$ . The notation  $\llbracket \cdot \rrbracket$  denotes the jump of a quantity across  $\Gamma$ . Specifically, for any  $x \in \Gamma$ ,

$$\begin{aligned} \llbracket u \rrbracket|_{\Gamma} &= \lim_{x \rightarrow \Gamma} u^+(x) - \lim_{x \rightarrow \Gamma} u^-(x) = w(x), \\ \llbracket \beta(x, u) \frac{\partial u}{\partial \mathbf{n}} \rrbracket|_{\Gamma} &= \lim_{x \rightarrow \Gamma} \beta^+(x, u^+) \nabla u^+ \cdot \mathbf{n} - \lim_{x \rightarrow \Gamma} \beta^-(x, u^-) \nabla u^- \cdot \mathbf{n} = v(x). \end{aligned} \quad (2)$$

Here,  $\mathbf{n}$  denotes the unit normal vector on  $\Gamma$  pointing from  $\Omega^+$  towards  $\Omega^-$ . The normal derivative of a function  $u$  is denoted by

$$\partial_{\mathbf{n}} u := \nabla u \cdot \mathbf{n}.$$

For brevity, in formulas we may also write  $\partial_n u$  when no confusion is possible.

The nonlinear diffusion coefficient  $\beta^{\pm}(x, \cdot)$  is a mapping  $\mathbb{R} \rightarrow \mathbb{R}$  that depends on  $u^{\pm}$ . We assume uniform ellipticity: there exists  $\delta > 0$  such that

$$\beta^{\pm}(x, s) \geq \delta, \quad \forall x \in \Omega, \quad \forall s \in \mathbb{R}. \quad (3)$$

Moreover,  $\beta^{\pm}$  is such that the associated nonlinear elliptic operator is strongly monotone: there exists  $\lambda^{\pm} > 0$  such that for all  $u, v \in H^1(\Omega^{\pm})$ ,

$$\int_{\Omega^{\pm}} (\beta^{\pm}(x, u) \nabla u - \beta^{\pm}(x, v) \nabla v) \cdot (\nabla u - \nabla v) dx \geq \lambda^{\pm} \|\nabla u - \nabla v\|_{L^2(\Omega^{\pm})}^2. \quad (4)$$

The source term  $f^{\pm}(x, s)$  is assumed to be Lipschitz continuous in  $s$ , i.e., there exist constants  $L_f^{\pm} > 0$  such that for all  $x \in \Omega^{\pm}$  and  $s, t \in \mathbb{R}$ ,

$$|f^{\pm}(x, s) - f^{\pm}(x, t)| \leq L_f^{\pm} |s - t|. \quad (5)$$

In order to absorb the  $L^2$ -error term via the Poincaré inequality in the subsequent error analysis, we further require that

$$L_f^{\pm} < \lambda^{\pm} / C_P^{\pm}, \quad (6)$$

where  $C_P^{\pm} > 0$  denotes the (optimal) Poincaré constant of  $\Omega^{\pm}$ .

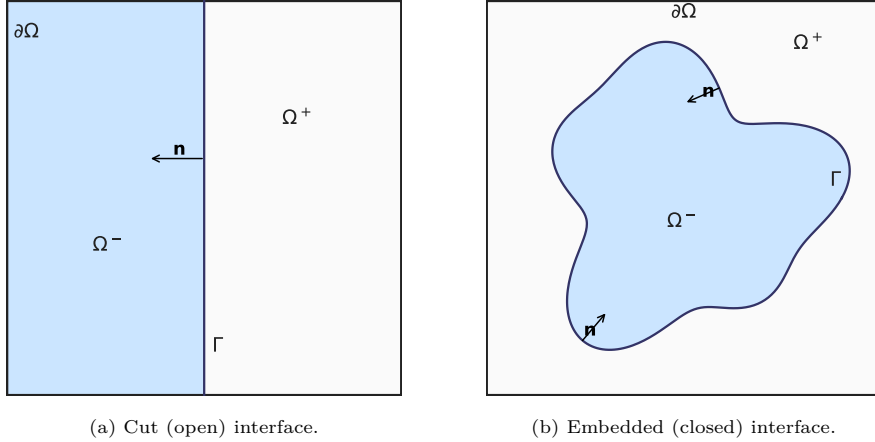


Figure 1: Two typical geometric configurations for interface problems. (a) A cut (open) interface that intersects the exterior boundary, partitioning the domain into disconnected subdomains. (b) An embedded (closed) interface located entirely within the domain, separating it into interior and exterior regions.

### 3. Methodology

In this section, we first present the concept and advantages of randomized neural networks. We then describe a method for solving nonlinear interface problems by integrating local randomized neural networks (LRaNNs) with a Newton-type iterative scheme. Finally, we introduce a perturbation-expansion strategy to address the nonlinear and nonconvex nature of the resulting optimization problem, thereby further improving the accuracy of the numerical solution.

#### 3.1. Local Randomized Neural Network (LRaNN) Architecture

Randomized Neural Networks (RaNNs) provide an efficient approach to function approximation, in which the hidden-layer parameters are randomly initialized and then kept fixed, while only the output-layer weights are optimized. In this work, we adopt a single-hidden-layer, fully connected feedforward architecture, as illustrated in Fig. 2. The network takes an input  $\mathbf{x} \in \mathbb{R}^d$ , passes it through  $m$  nonlinear neurons, and outputs a linear combination of their activations:

$$u(\mathbf{x}) = \sum_{j=1}^m \alpha_j \phi(\mathbf{w}_j \cdot \mathbf{x} + b_j) = \Phi(\mathbf{x})\boldsymbol{\alpha}, \quad (7)$$

where the weight vectors  $\mathbf{w}_j \in \mathbb{R}^d$  and bias vectors  $b_j \in \mathbb{R}$  are the randomly initialized and fixed input-to-hidden weights and biases,  $\phi(\cdot) : \mathbb{R} \rightarrow \mathbb{R}$  is a prescribed nonlinear activation function, and  $\alpha_j \in \mathbb{R}$  are the trainable output-layer coefficients collected in  $\boldsymbol{\alpha}$ .

As illustrated in Fig. 1, the computational domain  $\Omega$  is partitioned into several subdomains  $\Omega_i$  by the interface  $\Gamma$ . Across  $\Gamma$ , the PDE solution may exhibit discontinuities or reduced smoothness, which makes it challenging for a single neural network to capture the entire solution accurately. To address this, we employ a LRaNN framework in which one RaNN is assigned to each subdomain. The number of networks thus matches the number of subdomains.

For clarity, we focus on the case where  $\Omega$  is divided into two subdomains by  $\Gamma$ . To solve the nonlinear elliptic interface problem Eq. (1), we propose a LRaNN method that incorporates Newton iteration. In our approach, we select two LRaNNs  $u_N^+$  and  $u_N^-$  respectively on subdomains  $\Omega^+$  and  $\Omega^-$  to approximate the true solution. For simplicity, the number of neurons in the hidden layer of the two LRaNNs is assumed to be  $m$  for both networks. Similar to Eq. (7), we assume that the outputs of these two random neural networks

are given by the following formulas:

$$u_N^+ = \sum_{j=1}^m \alpha_j^+ \phi^+ (\mathbf{w}_j^+ \cdot \mathbf{x} + b_j^+), \quad u_N^- = \sum_{j=1}^m \alpha_j^- \phi^- (\mathbf{w}_j^- \cdot \mathbf{x} + b_j^-). \quad (8)$$

Here, the parameter vectors  $\boldsymbol{\alpha}^+ = (\alpha_1^+, \dots, \alpha_m^+)$  and  $\boldsymbol{\alpha}^- = (\alpha_1^-, \dots, \alpha_m^-)$  are the trainable output-layer coefficients for  $\Omega^+$  and  $\Omega^-$ , respectively. Each activation  $\phi(\mathbf{w}_j^\pm \cdot \mathbf{x} + b_j^\pm)$  serves as a basis function with randomly initialized weights  $\mathbf{w}_j^\pm$  and biases  $b_j^\pm$  fixed throughout the computation. These coefficients  $\boldsymbol{\alpha}^\pm$  are the primary unknowns to be updated in the Newton iterations described in the next subsection.

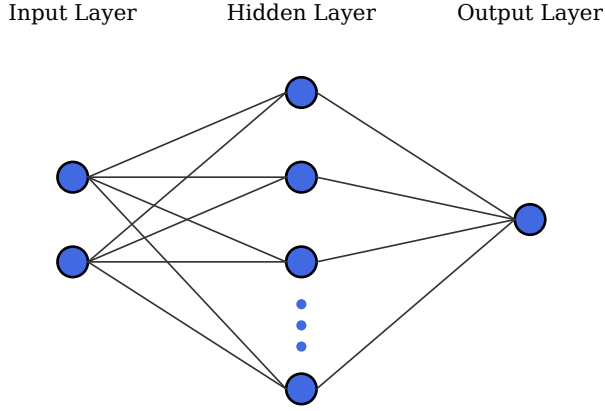


Figure 2: The structure of RaNN.

### 3.2. Discrete Least-Squares Functional

To incorporate the LRaNN approach into the solution of nonlinear interface problems, it is natural to recast the PDE system Eq. (1) as a minimization problem. In this subsection, we adopt a least-squares (LS) framework in which all governing equations, interface jump conditions, and boundary conditions are enforced by minimizing the sum of squared residuals.

Using the LRaNN approximations  $u_N^+$  and  $u_N^-$  defined in Eq. (8), we define the following residual functions:

For the interior of each subdomain, the residual corresponds to the violation of the governing PDE. Specifically, for  $x \in \Omega^+$  we define

$$\mathcal{R}_{\Omega^+}(x) := \nabla \cdot (\beta^+(x, u_N^+(x)) \nabla u_N^+(x)) + f^+(x, u_N^+(x)), \quad x \in \Omega^+,$$

whereas for  $x \in \Omega^-$  the corresponding expression is

$$\mathcal{R}_{\Omega^-}(x) := \nabla \cdot (\beta^-(x, u_N^-(x)) \nabla u_N^-(x)) + f^-(x, u_N^-(x)), \quad x \in \Omega^-.$$

Across the interface  $\Gamma$ , we define the residual for the jump conditions as

$$\mathcal{R}_{\Gamma_n}(x) := u_N^+(x) - u_N^-(x) - w(x), \quad x \in \Gamma,$$

and the residual for the flux jump

$$\mathcal{R}_{\Gamma_d}(x) := [\beta^+(x, u_N^+(x)) \partial_{\mathbf{n}} u_N^+(x) - \beta^-(x, u_N^-(x)) \partial_{\mathbf{n}} u_N^-(x)] - v(x), \quad x \in \Gamma.$$

On the outer boundary  $\partial\Omega$ , we impose Dirichlet conditions, with the residual

$$\mathcal{R}_{\partial\Omega}(x) := u_N^\pm(x) - g(x), \quad x \in \partial\Omega.$$

Collecting these definitions, we introduce the continuous least-squares functional

$$\begin{aligned} \min_{\boldsymbol{\alpha}} \frac{1}{2} \|\mathcal{F}(\boldsymbol{\alpha})\|_{L^2}^2 &= \min_{\boldsymbol{\alpha}} \left\{ \frac{\omega_{\Omega^+}}{2} \|\mathcal{R}_{\Omega^+}\|_{L^2}^2 + \frac{\omega_{\Omega^-}}{2} \|\mathcal{R}_{\Omega^-}\|_{L^2}^2 \right. \\ &\quad \left. \frac{\omega_{\Gamma_n}}{2} \|\mathcal{R}_{\Gamma_n}\|_{L^2}^2 + \frac{\omega_{\Gamma_d}}{2} \|\mathcal{R}_{\Gamma_d}\|_{L^2}^2 + \frac{\omega_{\partial\Omega}}{2} \|\mathcal{R}_{\partial\Omega}\|_{L^2}^2 \right\}, \end{aligned} \quad (9)$$

where  $\omega_{\Omega^+}$ ,  $\omega_{\Omega^-}$ ,  $\omega_{\Gamma_n}$ ,  $\omega_{\Gamma_d}$  and  $\omega_{\partial\Omega}$  are user-defined positive weights that can be tuned to balance the contributions of the different residual terms.

The  $L^2$  norms in Eq. (9) are approximated by Monte Carlo integration, using independent collections of collocation points sampled within each subdomain, interface, and boundary:

$$\begin{aligned} \mathcal{S}_{\Omega^+} &= \{x_i\}_{i=1}^{N_{\Omega^+}} \subseteq \Omega^+, \\ \mathcal{S}_{\Omega^-} &= \{x_i\}_{i=1}^{N_{\Omega^-}} \subseteq \Omega^-, \\ \mathcal{S}_\Gamma &= \{x_i\}_{i=1}^{N_\Gamma} \subseteq \Gamma, \\ \mathcal{S}_{\partial\Omega} &= \{x_i\}_{i=1}^{N_{\partial\Omega}} \subseteq \partial\Omega. \end{aligned} \quad (10)$$

Here,  $N_{\Omega^+}$ ,  $N_{\Omega^-}$ ,  $N_\Gamma$  and  $N_{\partial\Omega}$  denote the number of sample points in  $\Omega^+$ ,  $\Omega^-$ ,  $\Gamma$ , and  $\partial\Omega$ , respectively. By substituting these sample sets into the residual definitions, the least-squares problem Eq. (9) is discretized into

$$\begin{aligned} \frac{1}{2} \min_{\boldsymbol{\alpha}} \|\mathcal{F}(\boldsymbol{\alpha})\|_{l^2}^2 &= \frac{1}{2} \min_{\boldsymbol{\alpha}} \left\{ \frac{\omega_{\Omega^+}}{N_{\Omega^+}} \sum_{i=1}^{N_{\Omega^+}} |\mathcal{R}_{\Omega^+}(x_i; \boldsymbol{\alpha}^+)|^2 + \frac{\omega_{\Omega^-}}{N_{\Omega^-}} \sum_{i=1}^{N_{\Omega^-}} |\mathcal{R}_{\Omega^-}(x_i; \boldsymbol{\alpha}^-)|^2 \right. \\ &\quad + \frac{\omega_{\Gamma_n}}{N_{\Gamma_n}} \sum_{i=1}^{N_{\Gamma_n}} |\mathcal{R}_{\Gamma_n}(x_i; \boldsymbol{\alpha})|^2 + \frac{\omega_{\Gamma_d}}{N_{\Gamma_d}} \sum_{i=1}^{N_{\Gamma_d}} |\mathcal{R}_{\Gamma_d}(x_i; \boldsymbol{\alpha})|^2 \\ &\quad \left. + \frac{\omega_{\partial\Omega}}{N_{\partial\Omega}} \sum_{i=1}^{N_{\partial\Omega}} |\mathcal{R}_{\partial\Omega}(x_i; \boldsymbol{\alpha})|^2 \right\}. \end{aligned} \quad (11)$$

The optimal output-layer weights  $\boldsymbol{\alpha}$  are then obtained by solving the discrete least-squares problem Eq. (11).

### 3.3. Initialization Step

Building upon the LRaNNs introduced in Section 3.1 and the discrete least-squares formulation in Section 3.2, we now develop a Newton iterative scheme to solve the minimization problem

$$\min_{\boldsymbol{\alpha}} G(\boldsymbol{\alpha}) = \min_{\boldsymbol{\alpha}} \frac{1}{2} \|\mathcal{F}(\boldsymbol{\alpha})\|_{l^2}^2, \quad (12)$$

where  $\boldsymbol{\alpha} = (\boldsymbol{\alpha}^+, \boldsymbol{\alpha}^-)$  is the concatenated parameter vector. The global residual vector  $\mathcal{F} \in \mathbb{R}^{N_{\text{total}}}$ , where  $N_{\text{total}} = N_{\Omega^+} + N_{\Omega^-} + 2N_\Gamma + N_{\partial\Omega}$ , is formed by stacking the residuals evaluated at all collocation points Eq. (10), given by

$$\mathcal{F} = \begin{pmatrix} \mathcal{R}_{\Omega^+} \\ \mathcal{R}_{\Omega^-} \\ \mathcal{R}_{\Gamma_n} \\ \mathcal{R}_{\Gamma_d} \\ \mathcal{R}_{\partial\Omega} \end{pmatrix}. \quad (13)$$

To solve this nonlinear least-squares problem Eq. (12), we implement a regularized Gauss-Newton scheme. At iteration  $k$ , we approximate the Hessian matrix  $\nabla^2 G^{\{k\}} \approx \mathcal{J}^{\{k\}}^T \mathcal{J}^{\{k\}}$  where  $\mathcal{J}^{\{k\}} = \partial \mathcal{F}^{\{k\}} / \partial \boldsymbol{\alpha}$  is the Jacobian matrix, given by:

$$\mathcal{J} = \begin{pmatrix} \mathcal{J}_{\Omega^+} & \mathbf{0}_{N_{\Omega^+} \times m} \\ \mathbf{0}_{N_{\Omega^-} \times m} & \mathcal{J}_{\Omega^-} \\ \mathcal{J}_{\Gamma_n^+} & \mathcal{J}_{\Gamma_n^-} \\ \mathcal{J}_{\Gamma_d^+} & \mathcal{J}_{\Gamma_d^-} \\ \mathcal{J}_{\partial\Omega^+} & \mathbf{0}_{N_{\partial\Omega}^+ \times m} \\ \mathbf{0}_{N_{\partial\Omega}^- \times m} & \mathcal{J}_{\partial\Omega^-} \end{pmatrix}. \quad (14)$$

The  $\mathbf{0}$  matrices indicate that the corresponding residuals are independent of the coefficients from the other subdomain, and therefore the partial derivatives vanish identically. For brevity, we denote

$$\beta_u^\pm = \frac{\partial \beta^\pm}{\partial u}, \quad \beta_{uu}^\pm = \frac{\partial^2 \beta^\pm}{\partial u^2}, \quad f_u^\pm = \frac{\partial f^\pm}{\partial u}, \quad f_{uu}^\pm = \frac{\partial^2 f^\pm}{\partial u^2},$$

all evaluated at  $(x, u_N^\pm(x))$  unless otherwise stated.

The submatrices of the Jacobian matrix are defined pointwise at collocation locations Eq. (10). Here, for  $x_i \in \mathcal{S}_{\Omega^+}$  and activation function  $\phi_j^+$ , we define the submatrix  $\mathcal{J}_{\Omega^+}$

$$(\mathcal{J}_{\Omega^+})_{i,j} := \frac{\partial \mathcal{R}_{\Omega^+}}{\partial \alpha_j^+} \Big|_{x=x_i} = f_u^+ \phi_j^+ \Big|_{x=x_i} + \nabla \cdot (\beta_u^+ \phi_j^+ \nabla u_N^+) \Big|_{x=x_i} + \nabla \cdot (\beta^+ \nabla \phi_j^+) \Big|_{x=x_i}. \quad (15)$$

Similarly, the submatrix  $\mathcal{J}_{\Omega^-}$  is defined pointwise on  $x_i \in \mathcal{S}_{\Omega^-}$  with activation function  $\phi_j^-$ . Then, for  $x_i \in \mathcal{S}_\Gamma$  and activation function  $\phi_j^+$ , we can define the submatrix  $\mathcal{J}_{\Gamma_n^+}$  of the continuity condition

$$(\mathcal{J}_{\Gamma_n^+})_{i,j} := \frac{\partial \mathcal{R}_{\Gamma_n^+}}{\partial \alpha_j^+} \Big|_{x=x_i} = \phi_j^+ \Big|_{x=x_i}, \quad (16)$$

and we define  $\mathcal{J}_{\Gamma_d^+}$  of the flux jump condition

$$(\mathcal{J}_{\Gamma_d^+})_{i,j} := \frac{\partial \mathcal{R}_{\Gamma_d^+}}{\partial \alpha_j^+} \Big|_{x=x_i} = (\beta_u^+ \phi_j^+ \partial_{\mathbf{n}} u_N^+ + \beta^+ \partial_{\mathbf{n}} \phi_j^+) \Big|_{x=x_i}. \quad (17)$$

The blocks  $\mathcal{J}_{\Gamma_n^-}$  and  $\mathcal{J}_{\Gamma_d^-}$  are defined similarly for  $\phi_j^-$ . Finally, for  $x_i \in \mathcal{S}_{\partial\Omega}$  we derive the Jacobian submatrix  $\mathcal{J}_{\partial\Omega^\pm}$  corresponding to the boundary part

$$(\mathcal{J}_{\partial\Omega^\pm})_{i,j} := \frac{\partial \mathcal{R}_{\partial\Omega}}{\partial \alpha_j^\pm} \Big|_{x=x_i} = \phi_j^\pm \Big|_{x=x_i}. \quad (18)$$

The parameter update  $\delta\boldsymbol{\alpha} = (\delta\boldsymbol{\alpha}^+, \delta\boldsymbol{\alpha}^-)$  is computed by solving

$$\mathcal{J}^{\{k\}}^T \mathcal{J}^{\{k\}} \delta\boldsymbol{\alpha} = -\mathcal{J}^{\{k\}}^T \mathcal{F}^{\{k\}}, \quad (19)$$

where  $k$  denotes the iteration index. To ensure stable and efficient inversion, we compute  $\delta\boldsymbol{\alpha}$  via the singular value decomposition (SVD) and the corresponding Moore–Penrose pseudo-inverse  $\mathcal{J}^{\{k\}}$ . Specifically, let the SVD of  $\mathcal{J}^{\{k\}} \in \mathbb{R}^{N_{total} \times 2m}$  be

$$\mathcal{J}^{\{k\}} = U \Sigma V^T, \quad (20)$$

where  $U \in \mathbb{R}^{N_{total} \times r}$  and  $V \in \mathbb{R}^{2m \times r}$  are column-orthonormal matrices,  $\Sigma = \text{diag}\{\sigma_1, \sigma_2, \dots, \sigma_r, 0, \dots\}$  contains the nonzero singular values  $\sigma_1 \geq \sigma_2 \geq \dots \geq \sigma_r > 0$ , and  $r = \text{rank}(\mathcal{J}^{\{k\}})$ . In constructing the

pseudoinverse, we truncate all singular values  $\sigma_i$  smaller than a prescribed threshold  $\tau > 0$  and retain only those indices  $\mathcal{I}_r = \{i : \sigma_i \geq \tau\}$ . The truncated pseudoinverse of  $\Sigma$  is defined by

$$(\Sigma_r^\dagger)_{ii} = \begin{cases} 1/\sigma_i, & \sigma_i \geq \tau, \\ 0, & \sigma_i < \tau. \end{cases} \quad (21)$$

Accordingly, the regularized update is obtained as

$$\delta\boldsymbol{\alpha} = -V\Sigma_r^\dagger U^T \mathcal{F}^{\{k\}}. \quad (22)$$

Therefore, the output layer weights  $\boldsymbol{\alpha}$  is then updated by the standard Newton step

$$\boldsymbol{\alpha}^{\{k+1\}} = \boldsymbol{\alpha}^{\{k\}} + \delta\boldsymbol{\alpha}. \quad (23)$$

The iteration is terminated once the relative change in the residual norm satisfies

$$\frac{|\|\mathcal{F}(\boldsymbol{\alpha}^{\{k+1\}})\|_{l^2} - \|\mathcal{F}(\boldsymbol{\alpha}^{\{k\}})\|_{l^2}|}{\|\mathcal{F}(\boldsymbol{\alpha}^{\{k+1\}})\|_{l^2}} \leq \delta_0. \quad (24)$$

$\boldsymbol{\alpha}_0$  is a predefined initial value, for instance,  $\boldsymbol{\alpha}_0 = \mathbf{0}$ .

Crucially, the equivalence between solving the nonlinear system  $\mathcal{F}(\boldsymbol{\alpha}^+, \boldsymbol{\alpha}^-, \mathbf{x}) = \mathbf{0}$  and minimizing the functional  $G(\boldsymbol{\alpha}) = \frac{1}{2}\|\mathcal{F}(\boldsymbol{\alpha}^+, \boldsymbol{\alpha}^-, \mathbf{x})\|_{l^2}^2$  follows from the identity derived from the gradient  $\nabla_{\boldsymbol{\alpha}} G = \mathcal{J}^T \mathcal{F}$  and  $\mathcal{J}^T \mathcal{J}$  also serves as an approximation of the Hessian matrix in the optimization problem. This identity shows that the right-hand side  $\mathcal{J}^T \mathcal{F}$  of the linear system Eq. (19) is precisely the gradient of  $G$  with respect to  $\boldsymbol{\alpha}$ . However, due to the nonconvex nature of  $G(\boldsymbol{\alpha})$ , this optimization process may converge to local minima  $\boldsymbol{\alpha}^+$ ,  $\boldsymbol{\alpha}^-$ , and corresponding numerical solutions are given by

$$u_N^\pm = \sum_{j=1}^m \alpha_j^\pm \phi^\pm(\mathbf{w}_j^\pm \cdot \mathbf{x} + b_j^\pm). \quad (25)$$

### 3.4. The Perturbation–Correction Method

To further reduce the residuals remaining after the initialization step, we employ a perturbation–based correction strategy designed to exploit a locally quadratic approximation of the residual functional. Since the highly nonlinear and nonconvex nature of problem Eq. (1) can cause the Gauss–Newton iteration to converge to a local minimizer  $u_N^\pm$  with nonzero residuals, we seek to construct a refined solution of the form

$$u_g^\pm = u_N^\pm + \epsilon u_p^\pm, \quad \epsilon u_p^\pm \approx u_g^\pm - u_N^\pm = e^\pm, \quad (26)$$

where  $u_N^\pm$  is the LRNNs-based approximation obtained from the initialization step,  $\epsilon > 0$  is a small parameter proportional to the discrete residual norm  $\|\mathcal{F}(u_N)\|_{l^2}$ , and  $u_p^\pm$  represents the perturbation term. To ensure numerical stability and proper scaling of the correction term, we set the perturbation parameter  $\epsilon = \|\mathcal{F}(u_N)\|_{l^2}$ . This choice ensures that the unknown perturbation  $u_p$  remains  $O(1)$  in magnitude. By solving the perturbation subproblem for  $u_p^\pm$  to high accuracy, the correction  $\epsilon u_p^\pm$  yields a high-precision estimation of the true error  $e^\pm$ .

We note that, from the viewpoint of PDE structure, this perturbation equation is itself a nonlinear interface problem, possessing the same domain decomposition, jump conditions, and type of nonlinearities as the original model (1), but with a different right-hand side arising from the Taylor expansion around  $u_N^\pm$ . Therefore, the same LRNNs framework developed for the original problem can be applied directly to this perturbation subproblem.

Substituting the correction ansatz  $u_N^\pm + \epsilon u_p^\pm$  into the nonlinear residual operator  $\mathcal{F}(\cdot)$  and performing a Taylor expansion up to  $O(\epsilon^2)$ , yields

$$\mathcal{F}(u_N) + \epsilon \mathcal{F}'(u_N)[u_p] + \frac{1}{2}\epsilon^2 \mathcal{F}''(u_N)[u_p, u_p] + O(\epsilon^3).$$

Truncating at  $O(\epsilon^3)$  gives the perturbation equation

$$\mathcal{F}(u_N) + \epsilon \mathcal{F}'(u_N)[u_p] + \frac{1}{2}\epsilon^2 \mathcal{F}''(u_N)[u_p, u_p] \approx 0. \quad (27)$$

Equivalently, the least-squares functional  $G(\cdot)$  evaluated at the perturbed solution expands as

$$G(u_N + \epsilon u_p) = G(u_N) + \epsilon G'(u_N)[u_p] + \frac{1}{2}\epsilon^2 G''(u_N)[u_p, u_p] + O(\epsilon^3), \quad (28)$$

where  $G'$ ,  $G''$  denote the first and second Fréchet derivative, respectively.

For the ansatz of  $u_p^\pm$ , we also employ a LRaNNs-based architecture. Specifically,  $u_p^\pm$  is parameterized as a single-layer feedforward neural network with randomly fixed hidden-layer weights and biases, optimizing only the output-layer coefficients:

$$u_p^+ = \sum_{j=1}^m \gamma_j^+ \psi^+(\mathbf{w}_{pj}^+ \cdot \mathbf{x} + b_{pj}^+), \quad u_p^- = \sum_{j=1}^m \gamma_j^- \psi^-(\mathbf{w}_{pj}^- \cdot \mathbf{x} + b_{pj}^-), \quad (29)$$

where  $\psi^\pm$  are nonlinear activation functions (distinct from those in  $u_N^\pm$  for enhanced expressivity), and  $\mathbf{w}_{pj}^\pm, b_{pj}^\pm$  are randomly initialized and fixed. In the initialization step (Section 3.3), tanh activations are used, whereas in the correction step we employ sin activations to capture high-frequency components more effectively.

The vector  $\gamma = (\gamma^+, \gamma^-)$  is then optimized by solving the least-squares problem:

$$\min_{\gamma} G_p(\gamma) = \min_{\gamma} \left( G(u_N)/\epsilon + G'(u_N)[u_p(\gamma)] + \frac{1}{2}\epsilon G''(u_N)[u_p(\gamma), u_p(\gamma)] \right), \quad (30)$$

where  $\mathcal{F}_p$  is the discretized residual vector for the perturbation equation, comprising

$$\mathcal{F}_p = \frac{1}{\epsilon} \begin{pmatrix} \mathcal{R}_p^+ \\ \mathcal{R}_p^- \\ \mathcal{R}_{\Gamma_n, p} \\ \mathcal{R}_{\Gamma_d, p} \\ \mathcal{R}_{\partial\Omega, p} \end{pmatrix}, \quad (31)$$

evaluated at the collocation points  $\mathcal{S}_{\Omega^\pm}, \mathcal{S}_\Gamma, \mathcal{S}_{\partial\Omega}$ .

Explicitly, For each interior collocation point  $x_i \in \mathcal{S}_{\Omega^+}$ , the pointwise-defined perturbation residual  $\mathcal{R}_p^+(x_i)$  is

$$\begin{aligned} \mathcal{R}_p^+ = & \epsilon^0 \nabla \cdot (\beta^+(x_i, u_N^+) \nabla u_N^+ + f^+(x_i, u_N^+)) \\ & + \epsilon^1 (\nabla \cdot (\beta^+(x_i, u_N^+) \nabla u_p^+ + u_p^+ \beta_u^+(x_i, u_N^+) \nabla u_N^+) + u_p^+ f_u^+(x_i, u_N^+)) \\ & + \epsilon^2 \left( \nabla \cdot \left( \frac{1}{2} u_p^{+2} \beta_{uu}^+(x_i, u_N^+) \nabla u_N^+ + u_p^+ \beta_u^+(x_i, u_N^+) \nabla u_p \right) + \frac{1}{2} u_p^{+2} f_{uu}^+(x_i, u_N^+) \right). \end{aligned} \quad (32)$$

Here  $\epsilon^0, \epsilon^1, \epsilon^2$  indicate the contributions of zeroth-, first-, and second-order terms from the Taylor expansion. Analogously, for  $x_i \in \mathcal{S}_\Gamma$ , the residual with expressions for  $\mathcal{R}_p^-$ . For the interface conditions at  $x_i \in \mathcal{S}_\Gamma$ , we define the continuous condition

$$\mathcal{R}_{\Gamma_n, p} = u_N^+ - u_N^- - w(x_i) + \epsilon (u_p^+ - u_p^-), \quad (33)$$

and

$$\begin{aligned} \mathcal{R}_{\Gamma_d, p} = & \epsilon^0 (\beta^+(x_i, u_N^+) \partial_{\mathbf{n}} u_N^+ - \beta^-(x_i, u_N^-) \partial_{\mathbf{n}} u_N^- - v(x_i)) \\ & + \epsilon^1 (u_N^+ \beta_u^+(x_i, u_N^+) \partial_{\mathbf{n}} u_N^+ + \beta^+(x_i, u_N^+) \partial_{\mathbf{n}} u_p^+ - u_N^- \beta_u^-(x_i, u_N^-) \partial_{\mathbf{n}} u_N^- - \beta^-(x_i, u_N^-) \partial_{\mathbf{n}} u_p^-) \\ & + \epsilon^2 \left( u_N^+ \beta_u^+(x_i, u_N^+) \partial_{\mathbf{n}} u_p^+ + \frac{1}{2} u_p^{+2} \beta_{uu}^+(x_i, u_N^+) - u_N^- \beta_u^-(x_i, u_N^-) \partial_{\mathbf{n}} u_p^- \right. \\ & \left. - \frac{1}{2} u_p^{-2} \beta_{uu}^-(x_i, u_N^-) \right). \end{aligned} \quad (34)$$

On the boundary  $x_i \in \mathcal{S}_{\partial\Omega}$ , we define

$$\mathcal{R}_{\partial\Omega,p} = u_N^\pm - g(x_i) + \epsilon u_p^\pm. \quad (35)$$

The Gauss–Newton Jacobian is the block matrix

$$\mathcal{J}_p = \frac{\partial \mathcal{F}_p}{\partial \gamma} = \frac{1}{\epsilon} \begin{pmatrix} \mathcal{J}_{\Omega^+,p} & 0 \\ 0 & \mathcal{J}_{\Omega^-,p} \\ \mathcal{J}_{\Gamma_n,p}^+ & \mathcal{J}_{\Gamma_n,p}^- \\ \mathcal{J}_{\Gamma_d,p}^+ & \mathcal{J}_{\Gamma_d,p}^- \\ \mathcal{J}_{\partial\Omega,p}^+ & 0 \\ 0 & \mathcal{J}_{\partial\Omega,p}^- \end{pmatrix}, \quad (36)$$

with pointwise-defined submatrices evaluated at the collocation sets  $S_{\Omega^\pm}$ ,  $S_\Gamma$ , and  $S_{\partial\Omega}$ . Below we give the submatrices explicitly. For  $x_i \in S_{\Omega^+}$ , the  $i,j$  entry of  $J_{\Omega^+,p} \in \mathbb{R}^{N_{\Omega^+} \times m}$  is

$$\begin{aligned} (\mathcal{J}_{\Omega^+,p})_{i,j} &= \frac{\partial \mathcal{R}_p^+(x_i)}{\partial \gamma_j^+} \Big|_{x=x_i} \\ &= \epsilon^1 \left( \nabla \cdot (\beta^+ \nabla \psi_j^+) + \nabla \cdot (\beta_u^+ \psi_j^+ \nabla u_N^+) + f_u^+ \psi_j^+ \right) \Big|_{x=x_i} \\ &\quad + \epsilon^2 \left( \nabla \cdot (u_p^+ \psi_j^+ \beta_{uu}^+ \nabla u_N^+) + \nabla \cdot (\beta_u^+ \psi_j^+ \nabla u_p^+) + \nabla \cdot (\beta_u^+ u_p^+ \nabla \psi_j^+) + f_{uu}^+ u_p^+ \psi_j^+ \right) \Big|_{x=x_i}. \end{aligned} \quad (37)$$

The block  $J_{\Omega^-,p}$  is analogous with  $(+)$  replaced by  $(-)$  and basis functions  $\psi_j^-$ . For  $x_i \in S_\Gamma$ ,

$$\begin{aligned} (\mathcal{J}_{\Gamma_n,p}^+)_i{}_j &= \frac{\partial \mathcal{R}_{\Gamma_n,p}(x_i)}{\partial \gamma_j^+} \Big|_{x=x_i} = \epsilon \psi_j^+(x_i), \\ (\mathcal{J}_{\Gamma_n,p}^-)_i{}_j &= \frac{\partial \mathcal{R}_{\Gamma_n,p}(x_i)}{\partial \gamma_j^-} \Big|_{x=x_i} = -\epsilon \psi_j^-(x_i). \end{aligned} \quad (38)$$

For  $x_i \in S_\Gamma$ , the  $\epsilon^0$ -part of  $\mathcal{R}_{\Gamma_d,p}$  does not depend on  $\gamma$ , hence contributes nothing to the Jacobian. Using the residual definition, the  $\epsilon$ - and  $\epsilon^2$ -contributions yield

$$\begin{aligned} (\mathcal{J}_{\Gamma_d,p}^+)_i{}_j &= \epsilon \beta^+ \partial_{\mathbf{n}} \psi_j^+ + \epsilon^2 \left( u_N^+ \beta_u^+ \partial_{\mathbf{n}} \psi_j^+ + u_p^+ \psi_j^+ \beta_{uu}^+ \right), \\ (\mathcal{J}_{\Gamma_d,p}^-)_i{}_j &= -\epsilon \beta^- \partial_{\mathbf{n}} \psi_j^- + \epsilon^2 \left( -u_N^- \beta_u^- \partial_{\mathbf{n}} \psi_j^- - u_p^- \psi_j^- \beta_{uu}^- \right). \end{aligned} \quad (39)$$

For  $x_i \in S_{\partial\Omega} \cap \partial\Omega^\pm$ ,

$$(J_{\partial\Omega,p}^\pm)_{i,j} = \frac{\partial \mathcal{R}_{\partial\Omega,p}(x_i)}{\partial \gamma_j^\pm} = \epsilon \psi_j^\pm(x_i). \quad (40)$$

With the explicit construction of the perturbation residual vector  $\mathcal{F}_p$ , the associated least-squares subproblem Eq. (30) can then be efficiently minimized via the Gauss–Newton scheme, as in the initialization step. Integrating both steps, we summarize the complete two-step optimization procedure in the following algorithm. This two-stage strategy not only improves solution accuracy but, as will be shown in Section 4.2, yields a convex subproblem for the correction step, ensuring robust convergence and error control.

**Remark 1.** *The Gauss–Newton method employed for minimizing the discrete functional  $G(\boldsymbol{\alpha}) = \frac{1}{2} \|\mathcal{F}(\boldsymbol{\alpha})\|_{l^2}^2$  is mathematically equivalent to Newton’s method for solving the nonlinear residual system  $\mathcal{F}(\boldsymbol{\alpha}) = \mathbf{0}$ . This stems from the gradient relation  $\nabla_{\boldsymbol{\alpha}} G = \mathcal{J}^T \mathcal{F}$ , where  $\mathcal{J} = \partial \mathcal{F} / \partial \boldsymbol{\alpha}$  is the Jacobian matrix, and the approximation of the Hessian matrix by  $\mathcal{J}^T \mathcal{J}$ . Consequently, the update step in minimization solves the normal equations  $\mathcal{J}^T \mathcal{J} \delta \boldsymbol{\alpha} = -\mathcal{J}^T \mathcal{F}$ , while the direct Newton update for root-finding solves  $\mathcal{J} \delta \boldsymbol{\alpha} = -\mathcal{F}$ . The former*

---

**Algorithm 1** LRaNN–Newton–Perturbation Framework

---

- 1: Initialize random neural networks:  $u_N^\pm = \sum_{j=1}^m \alpha_j^\pm \phi^\pm (\mathbf{w}_j \cdot \mathbf{x} + \mathbf{b}_j)$  for  $\mathbf{x} \subseteq \bar{\Omega}$ .
- 2: **for**  $k = 1$  to  $M$  **do**
- 3:   Calculate the residual vector  $\mathcal{F}(\boldsymbol{\alpha})$  and the Jacobian matrix  $\mathcal{J}(\boldsymbol{\alpha})$  of Eq. (1).
- 4:   Solve the normal equations  $\mathcal{J}\delta\boldsymbol{\alpha} = -\mathcal{F}$  and update the weight vector  $\boldsymbol{\alpha}^{l_{k+1}} = \boldsymbol{\alpha}^{\{k\}} + \delta\boldsymbol{\alpha}$ .
- 5:   Repeat 3 and 4 until the residuals converge Eq. (24) or the iteration ends.
- 6: **end for**
- 7: Obtain the numerical solution  $u_N^\pm$  and calculate the governing equation of the perturbation expansion term  $u_p^\pm$ .
- 8: Initialize random neural networks:  $u_p^\pm = \sum_{j=1}^m \gamma_j^\pm \psi^\pm (\mathbf{w}_{pj}^\pm \cdot \mathbf{x} + b_{pj}^\pm)$  for  $\mathbf{x} \subseteq \bar{\Omega}$ .
- 9: **for**  $k = 1$  to  $M$  **do**
- 10:   Calculate the residual vector  $\mathcal{F}_p(\boldsymbol{\gamma})$  and the Jacobian matrix  $\mathcal{J}_p(\boldsymbol{\gamma})$  of the governing equation of the perturbation expansion term  $u_p^\pm$ .
- 11:   Solve the normal equations  $\mathcal{J}_p\delta\boldsymbol{\gamma} = -\mathcal{F}_p$  and update the weight vector  $\boldsymbol{\gamma}^{\{k+1\}} = \boldsymbol{\gamma}^{\{k\}} + \delta\boldsymbol{\gamma}$ .
- 12:   Repeat 10 and 11 until the residuals converge or the iteration ends.
- 13: **end for**
- 14: Obtain the final solution  $u^\pm = u_N^\pm(\boldsymbol{\alpha}) + \epsilon u_p^\pm(\boldsymbol{\gamma})$ .

---

provides regularization through the least-squares structure, enhancing stability for overdetermined systems. This equivalence extends identically to the perturbation subproblem, where minimizing  $G_p(\boldsymbol{\gamma}) = \frac{1}{2} \|\mathcal{F}_p(\boldsymbol{\gamma})\|_{l^2}^2$  or solving  $\mathcal{F}_p(\boldsymbol{\gamma}) = \mathbf{0}$  follows the same forms with Jacobian matrix  $\mathcal{J}_p$  and residual vector  $\mathcal{F}_p$ , as detailed in Eq. (31).

**Remark 2.** In the computation of the Jacobian matrix  $J(\boldsymbol{\alpha})$  and the residual vector  $\mathcal{F}(\boldsymbol{\alpha})$  within the LRaNN–Newton framework, two primary optimization strategies can be employed. First, leveraging the explicit expression of the ELM approximation  $u_N^\pm = \sum_{j=1}^m \alpha_j^\pm \phi^\pm (w_j \cdot x + b_j)$  for  $x \in \bar{\Omega}$ , the divergence operator in the governing equation can be analytically expanded. This approach allows for direct symbolic differentiation, yielding exact expressions for the partial derivatives without numerical approximation errors, which is particularly advantageous for maintaining precision in the Newton updates. Alternatively, automatic differentiation techniques, commonly utilized in deep learning frameworks, can be adopted to compute the required gradients algorithmically. However, this method incurs a higher computational cost due to the overhead of forward and backward passes through the computational graph, especially for large-scale problems or when higher-order derivatives are involved. The choice between these methods depends on the trade-off between computational efficiency and implementation simplicity in practical scenarios.

#### 4. Error Analysis

In this section, we present an error analysis framework for the two-step optimization applied to quasi-linear elliptic interface problems. First, we establish that the upper bound for the  $L^2$  errors of the gradients  $\nabla e^\pm$  is linked to the least-squares objective Eq. (9). Next, we connect the continuous  $L^2$ -norms of the residuals with their discrete ( $l^2$ ) counterparts, providing an explicit bound that accounts for the quadrature error. Finally, we prove that the correction step transforms the original nonconvex optimization problem into a convex quadratic subproblem, and we characterize the truncation error associated with the perturbation expansion. This theoretical foundation will be confirmed by the numerical experiments in Section 5.

##### 4.1. Generalization error estimation

Let  $u_h = (u_h^+, u_h^-)$  denote the current numerical solution obtained from the two-step optimization procedure, and let  $u_g = (u_g^+, u_g^-)$  be the exact solution of Eq. (1). In the initialization step,  $u_h$  coincides with the Newton-optimized LRaNN approximation,

$$u_h = u_N = (u_N^+, u_N^-),$$

while in the correction step it is updated to

$$u_h = u_N + \epsilon u_p,$$

where  $u_p = (u_p^+, u_p^-)$  denotes the perturbation network from Eq. (30), and  $\epsilon > 0$  is the small scaling parameter controlling the correction magnitude. The error bounds derived in this section therefore apply to either stage of the algorithm, and the comparison between the two cases quantifies the effect of the correction step. Define the local errors  $e_h^\pm := u_g^\pm - u_h^\pm$ . Subtracting the exact and numerical equations for  $u^+$  in  $\Omega^+$  yields the PDE residual equation in that subdomain:

$$-\nabla \cdot (\beta^+(x, u_g^+) \nabla u_g^+ - \beta^+(x, u_h^+) \nabla u_h^+) = f^+(x, u_g^+) - f^+(x, u_h^+) - R_{\Omega^+}. \quad (41)$$

Testing with  $e^+$  and integrating over  $\Omega^+$  gives

$$\begin{aligned} & \int_{\Omega^+} (\beta^+(x, u_g^+) \nabla u_g^+ - \beta^+(x, u_h^+) \nabla u_h^+) \cdot \nabla e^+ \, dx \\ &= \int_{\partial\Omega} [\beta^+(x, u_g^+) \partial_{\mathbf{n}^+} u_g^+ - \beta^+(x, u_h^+) \partial_{\mathbf{n}^+} u_h^+] e^+ \, ds \\ & \quad + \int_{\Gamma} [\beta^+(x, u_g^+) \partial_{\mathbf{n}^+} u_g^+ - \beta^+(x, u_h^+) \partial_{\mathbf{n}^+} u_h^+] e^+ \, ds \\ & \quad + \int_{\Omega^+} (f^+(x, u_g^+) - f^+(x, u_h^+)) e^+ \, dx - \int_{\Omega^+} R_{\Omega^+} e^+ \, dx. \end{aligned} \quad (42)$$

By Hölder inequality and Young inequality, the residual term  $\mathcal{R}_{\Omega^+}$  on subdomain  $\Omega^+$  satisfies

$$\left| \int_{\Omega^+} R_{\Omega^+} e^+ \, dx \right| \leq \frac{1}{2\eta} \|R_{\Omega^+}\|_{L^2(\Omega^+)}^2 + \frac{\eta}{2} \|e^+\|_{L^2(\Omega^+)}^2, \quad \forall \eta > 0.$$

The boundary integral on  $\partial\Omega^+$  similarly yields

$$\begin{aligned} & \left| \int_{\partial\Omega} [\beta^+(x, u_g^+) \partial_{\mathbf{n}^+} u_g^+ - \beta^+(x, u_h^+) \partial_{\mathbf{n}^+} u_h^+] \mathcal{R}_{\partial\Omega} \, ds \right| \\ & \leq \|R_{\partial\Omega}\|_{L^2(\partial\Omega)} (\|\beta^+(x, u_g^+) \nabla u_g^+\| + \|\beta^+(x, u_h^+) \nabla u_h^+\|) \\ & \leq C \|\mathcal{R}_{\partial\Omega}\|. \end{aligned}$$

Using the strong monotonicity assumption Eq. (4) for  $\beta^+$  and the Lipschitz property of  $f^+$  Eqs. (5) and (6), yielding

$$\|\nabla e^+\|_{L^2(\Omega^+)}^2 \leq C \left( \|\mathcal{R}_{\partial\Omega}\|_{L^2(\partial\Omega)} + \|\mathcal{R}_{\Omega^+}\|_{L^2(\Omega^+)}^2 \right) + \int_{\Gamma} [\beta^+(x, u_g^+) \partial_{\mathbf{n}^+} u_g^+ - \beta^+(x, u_h^+) \partial_{\mathbf{n}^+} u_h^+] e^+ \, ds. \quad (43)$$

The estimate Eq. (43) shows that, for  $\Omega^+$ , the  $H^1$  seminorm of the local error is bounded in terms of the interior equation residual, the boundary residual, and an interface contribution. Applying the same steps on  $\Omega^-$  yields

$$\|\nabla e^-\|_{L^2(\Omega^-)}^2 \leq C \|\mathcal{R}_{\Omega^-}\|_{L^2(\Omega^-)}^2 - \int_{\Gamma} [\beta^-(x, u_g^-) \partial_{\mathbf{n}^-} u_g^- - \beta^-(x, u_h^-) \partial_{\mathbf{n}^-} u_h^-] e^- \, ds. \quad (44)$$

Here, the first term on the right controls the interior PDE contribution, while the second term couples the subdomain errors through interface fluxes. Consider the continuity conditions and flux conditions on the interface

$$\begin{aligned} u_h^+ - u_h^- - w(x) &= \mathcal{R}_{\Gamma_n}, \quad x \in \Gamma, \\ \beta^+(x, u_h^+) \partial_{\mathbf{n}} u_h^+ - \beta^-(x, u_h^-) \partial_{\mathbf{n}} u_h^- - v(x) &= \mathcal{R}_{\Gamma_d}, \quad x \in \Gamma, \end{aligned} \quad (45)$$

and we denote

$$B_\Gamma^+ = \beta^+(x, u_g^+) \partial_{\mathbf{n}} u_g^+ - \beta^+(x, u_h^+) \partial_{\mathbf{n}} u_h^+, \quad B_\Gamma^- = \beta^-(x, u_g^-) \partial_{\mathbf{n}} u_g^- - \beta^-(x, u_h^-) \partial_{\mathbf{n}} u_h^-. \quad (46)$$

We add the integral at the interface Eq. (43) and Eq. (44), and obtain

$$\begin{aligned} \int_{\Gamma} (B_\Gamma^+ e^+ - B_\Gamma^- e^-) \, ds &= \int_{\Gamma} ((B_\Gamma^- - \mathcal{R}_{\Gamma_d}) (e^- - \mathcal{R}_{\Gamma_n}) - B_\Gamma^- e^-) \, ds \\ &= \int_{\Gamma} (\mathcal{R}_{\Gamma_d} \mathcal{R}_{\Gamma_n} - e^- \mathcal{R}_{\Gamma_d} - B_\Gamma^- \mathcal{R}_{\Gamma_n}) \, ds \\ &\leq \frac{1}{2} \|\mathcal{R}_{\Gamma_n}\|_{L^2(\Gamma)}^2 + \frac{1}{2} \|\mathcal{R}_{\Gamma_d}\|_{L^2(\Gamma)}^2 + C (\|\mathcal{R}_{\Gamma_n}\|_{L^2(\Gamma)} + \|\mathcal{R}_{\Gamma_d}\|_{L^2(\Gamma)}). \end{aligned} \quad (47)$$

Therefore, by adding inequalities Eq. (43) and Eq. (44), incorporating estimation Eq. (47) at the interface, we obtain the estimation:

$$\begin{aligned} \|\nabla e^+\|_{L^2(\Omega^+)}^2 + \|\nabla e^-\|_{L^2(\Omega^-)}^2 &\leq C \left( \|\mathcal{R}_{\Omega^+}\|_{L^2(\Omega^+)}^2 + \|\mathcal{R}_{\Omega^-}\|_{L^2(\Omega^-)}^2 + \|\mathcal{R}_{\partial\Omega}\|_{L^2(\partial\Omega)}^2 + \right. \\ &\quad \left. \|\mathcal{R}_{\Gamma_n}\|_{L^2(\Gamma)}^2 + \|\mathcal{R}_{\Gamma_d}\|_{L^2(\Gamma)}^2 + \|\mathcal{R}_{\Gamma_n}\|_{L^2(\Gamma)} + \|\mathcal{R}_{\Gamma_d}\|_{L^2(\Gamma)} \right). \end{aligned} \quad (48)$$

After deriving the continuous energy estimate in Eq. (48), we relate the continuous  $L^2$ -norms of the residuals to their discrete counterparts. Namely, for any sufficiently regular residual  $r = \{\mathcal{R}_{\Omega^+}, \mathcal{R}_{\Omega^-}, \mathcal{R}_{\Gamma_n}, \mathcal{R}_{\Gamma_d}, \mathcal{R}_{\partial\Omega}\}$  defined on  $D = \{\mathcal{S}_{\Omega^+}, \mathcal{S}_{\Omega^-}, \mathcal{S}_{\Gamma}, \mathcal{S}_{\partial\Omega}\}$  in Eq. (10), we have

$$\|r\|_{L^2(D)}^2 \leq \|r\|_{l^2(D)}^2 + C_{\text{quad}}^D N_D^{-\alpha_D}, \quad (49)$$

where  $\|r\|_{l^2(D)}^2 = \frac{1}{N_D} \sum_{n=1}^{N_D} |r(x_n^D)|^2$ , and the quadrature constants  $C_{\text{quad}}^D$  and exponents  $\alpha_D$  depend on the quadrature rule (cf. Eq. (2.6)–(2.7) in [58]). Consequently,

$$\|r\|_{L^2(D)} \leq \|r\|_{N_D} + (C_{\text{quad}}^D)^{1/2} N_D^{-\alpha_D/2}. \quad (50)$$

Thus, the continuous norms in (4.8) can be controlled by the discrete (empirical) norms, up to a quadrature error. Namely,

$$\begin{aligned} \|\nabla e^+\|_{L^2(\Omega^+)}^2 + \|\nabla e^-\|_{L^2(\Omega^-)}^2 &\leq C_1 \left( \|\mathcal{R}_{\Omega^+}\|_{l^2(\Omega^+)}^2 + \|\mathcal{R}_{\Omega^-}\|_{l^2(\Omega^-)}^2 + \|\mathcal{R}_{\partial\Omega}\|_{l^2(\partial\Omega)}^2 + \right. \\ &\quad \left. \|\mathcal{R}_{\Gamma_n}\|_{l^2(\Gamma)}^2 + \|\mathcal{R}_{\Gamma_d}\|_{l^2(\Gamma)}^2 + \|\mathcal{R}_{\Gamma_n}\|_{l^2(\Gamma)} + \|\mathcal{R}_{\Gamma_d}\|_{l^2(\Gamma)} \right) + \\ &\quad C_2 \left( N^{-\alpha_{\Omega^+}} + N^{-\alpha_{\Omega^-}} + N^{-\alpha_{\partial\Omega}/2} + N^{-\alpha_{\Gamma_n}} + N^{-\alpha_{\Gamma_d}} + \right. \\ &\quad \left. N^{-\alpha_{\Gamma_n}/2} + N^{-\alpha_{\Gamma_d}/2} \right). \end{aligned} \quad (51)$$

#### 4.2. Convexity Analysis of Perturbed Subproblems

Recall that the perturbations  $u_p^\pm$  are parameterized by the single-hidden-layer LRaNN ansatz introduced in Eq. (7). With the hidden weights and biases randomly initialized and then frozen, the map  $\gamma \mapsto u_p^\pm(\gamma)$  is linear. Suppose that the initialization step Newton iteration delivers an iterate  $u_N^\pm(\alpha)$  that lies in a neighborhood of a local minimizer  $u_*^\pm$  of  $G$ , so that  $G'(u_N)$  is small and  $G''(u_N)$  is positive semidefinite. Under this assumption, the reduced Hessian  $\langle u_p^\pm, G''(u_N^\pm) u_p^\pm \rangle$  is positive semidefinite, hence the objective in Eq. (30) is a convex quadratic in  $\gamma$  over the parameter space  $\mathbb{R}^{2m}$ .

Let  $G$  denote the objective functional in Eq. (12), with initialization step solution  $u_N^\pm$ , and let  $u_p^\pm = u_p^\pm(\gamma)$  denote the optimized perturbation obtained by minimizing the truncated quadratic model  $G_p(\gamma)$  as described in Eq. (30). Let  $\epsilon > 0$  be the small perturbation parameter, typically chosen such that  $\epsilon = O(\|G'(u_N)\|)$ , reflecting the initialization step convergence. We define the correction solution as

$$u_h^\pm := u_N^\pm + \epsilon u_p^\pm.$$

Expanding the objective  $G$  around  $u_N$  for the solution  $u_h = u_N + \epsilon u_p$  yields

$$G(u_h) = G(u_N) + \epsilon \langle G'(u_N), u_p \rangle + \frac{\epsilon^2}{2} \langle u_p, G''(u_N) u_p \rangle + O(\epsilon^3). \quad (52)$$

In contrast, the optimized value of the truncated subproblem is

$$\epsilon G_p(u_p) = G(u_N) + \epsilon \langle G'(u_N), u_p \rangle + \frac{\epsilon^2}{2} \langle u_p, G''(u_N) u_p \rangle. \quad (53)$$

Comparing with the Taylor expansion Eq. (52), we see that

$$G(u_h) = \epsilon G_p(u_p) + O(\epsilon^3), \quad (54)$$

so that the reduction predicted by the truncated quadratic model  $G_p$  is realized up to a controllable third-order term in  $\epsilon$ .

From Eq. (51), the initialization step solution  $u_N^\pm$  satisfies

$$\begin{aligned} & \|\nabla(u_g^+ - u_N^+)\|_{L^2(\Omega^+)}^2 + \|\nabla(u_g^- - u_N^-)\|_{L^2(\Omega^-)}^2 \\ & \leq C_1 \left( \|\mathcal{R}_{\Omega^+}(u_N)\|_{l^2(\Omega^+)}^2 + \|\mathcal{R}_{\Omega^-}(u_N)\|_{l^2(\Omega^-)}^2 + \|\mathcal{R}_{\partial\Omega}(u_N)\|_{l^2(\partial\Omega)}^2 \right. \\ & \quad \left. + \|\mathcal{R}_{\Gamma_n}(u_N)\|_{l^2(\Gamma)}^2 + \|\mathcal{R}_{\Gamma_d}(u_N)\|_{l^2(\Gamma)}^2 + \|\mathcal{R}_{\Gamma_n}(u_N)\|_{l^2(\Gamma)} + \|\mathcal{R}_{\Gamma_d}(u_N)\|_{l^2(\Gamma)} \right) \\ & \quad + C_2 \left( N^{-\alpha_{\Omega^+}} + N^{-\alpha_{\Omega^-}} + N^{-\alpha_{\partial\Omega}/2} + N^{-\alpha_{\Gamma_n}} + N^{-\alpha_{\Gamma_d}} + N^{-\alpha_{\Gamma_n}/2} + N^{-\alpha_{\Gamma_d}/2} \right). \end{aligned} \quad (55)$$

The quadrature error term (coefficient  $C_2$ ) depends only on the integration rule and the smoothness of the residuals.

For  $u_h^\pm = u_N^\pm + \epsilon u_p^\pm$ , the error bound takes the same form:

$$\begin{aligned} & \|\nabla(u_g^+ - u_h^+)\|_{L^2(\Omega^+)}^2 + \|\nabla(u_g^- - u_h^-)\|_{L^2(\Omega^-)}^2 \\ & \leq C_1 \left( \|\mathcal{R}_{\Omega^+}(u_h)\|_{l^2(\Omega^+)}^2 + \|\mathcal{R}_{\Omega^-}(u_h)\|_{l^2(\Omega^-)}^2 + \|\mathcal{R}_{\partial\Omega}(u_h)\|_{l^2(\partial\Omega)}^2 \right. \\ & \quad \left. + \|\mathcal{R}_{\Gamma_n}(u_h)\|_{l^2(\Gamma)}^2 + \|\mathcal{R}_{\Gamma_d}(u_h)\|_{l^2(\Gamma)}^2 + \|\mathcal{R}_{\Gamma_n}(u_h)\|_{l^2(\Gamma)} + \|\mathcal{R}_{\Gamma_d}(u_h)\|_{l^2(\Gamma)} \right) \\ & \quad + C_2 \left( N^{-\alpha_{\Omega^+}} + N^{-\alpha_{\Omega^-}} + N^{-\alpha_{\partial\Omega}/2} + N^{-\alpha_{\Gamma_n}} + N^{-\alpha_{\Gamma_d}} + N^{-\alpha_{\Gamma_n}/2} + N^{-\alpha_{\Gamma_d}/2} \right) + O(\epsilon^3). \end{aligned} \quad (56)$$

Here, the additional  $O(\epsilon^3)$  term represents the *truncation error* stemming from the use of the quadratic model  $G_p$  instead of the exact functional  $G$  in the correction step (cf. Eq. (52)). From the convex quadratic minimization, each discrete residual norm  $\|\mathcal{R}_D(u_h)\|_{l^2(D)}$  is reduced compared to  $\|\mathcal{R}_D(u_N)\|_{l^2(D)}$ , up to this  $O(\epsilon^3)$  effect. Therefore, the  $C_1$ -term in Eq. (56) is strictly smaller than in Eq. (55), the  $C_2$ -term (integration error) is identical, and the only new contribution is the controllable cubic-order truncation error.

It is important to remark that, while the perturbation subproblem retains the topological structure of the original interface problem—including the domain decomposition and jump conditions—it exhibits significantly attenuated nonlinearity compared to the original PDE. Specifically, once the initialization  $u_N$  is fixed, the optimization landscape for  $u_p$  is governed by the truncated local quadratic model, rendering the computational cost largely independent of the complexity of the coefficient  $\beta$ . Consequently, the correction step remains numerically stable and efficient, ensuring the rapid convergence rates that are empirically substantiated in the numerical experiments of Section 5.

## 5. Numerical examples

In this section, we evaluate the performance of the proposed perturbation–correction method through a series of quasi-linear interface problems. In all experiments, the Initialization Step corresponds to the direct

application of the LRaNNs solver: the solution  $u_N$  is obtained by minimizing the least-squares residual on a fixed randomized basis via the Gauss–Newton method introduced in Section 3.3. The Correction Step then computes the perturbation  $u_p$  introduced in Section 3.4 to refine the approximation. Consequently, the comparison between these two stages quantifies the specific gain offered by the Perturbation–Correction Method over the standard randomized neural network baseline. The selected tests cover steady and unsteady cases, multiple and curved interfaces, different types of nonlinear diffusion (including dependence on  $u$ , on  $|\nabla u|$ , and mixed forms), as well as scenarios with high contrast. To quantify the solution accuracy, the relative  $L^2$  error and relative  $L^\infty$  error are defined on a uniformly distributed test set as

$$error_{L^2} = \frac{\sqrt{\sum_{i=1}^N (u_g - u_h)^2}}{\sqrt{\sum_{i=1}^N u_g^2}}, \quad error_{L^\infty} = \frac{\max_{x_i} |u_g(x_i) - u_h(x_i)|}{\max_{x_i} |u_g(x_i)|}. \quad (57)$$

### 5.1. Example 1

In this numerical example, we consider a class of heat conduction equations with different materials with homogeneous jump conditions, namely,  $w = v = 0$ . The computational domain is  $\Omega = [-1, 1] \times [0, 1]$ , and the interface

$$\Gamma = \{(x, y) \mid x = 0\}$$

splits  $\Omega$  into the left subdomain  $\Omega^- = [-1, 0] \times [0, 1]$  and the right subdomain  $\Omega^+ = [0, 1] \times [0, 1]$ . The nonlinear diffusion coefficient is defined piecewise as

$$\beta(x, u) = \begin{cases} 1 + u, & x \in \Omega^-, \\ 1 + \frac{1}{2}u^2, & x \in \Omega^+, \end{cases}$$

and the source terms  $f^\pm(x, u)$  are chosen so that the exact solution is

$$u(x, y) = \begin{cases} x^2 y^2, & x \in \Omega^-, \\ e^{-x} x^2 y^2, & x \in \Omega^+. \end{cases}$$

We first apply the initialization-step Newton iteration scheme to this nonlinear interface problem. In the initialization step, LRaNNs with  $m = 100$  hidden neurons and tanh activation in each subdomain are employed. Network weights and biases are initialized from uniform distributions  $w \in [-1, 1]^2$  and  $b \in [-0.1, 0.1]$ . For the discrete least-squares formulation, a total of 21,816 collocation points are used to ensure accurate quadrature of the residual functional.

The Newton solver exhibits rapid convergence, reaching a stable solution within 5 iterations, as depicted in the first half of Fig. 3c. However, the process converges to a local minimum, beyond which no further improvement is observed. This stagnation phenomenon is clearly depicted in Fig. 3c, where the residual norm is shown to plateau. Consequently, the relative  $L^2$  error stabilizes at  $O(10^{-7})$ . The spatial distribution of this pointwise error, visualized in Fig. 3, reveals a persistent, structured residual. This result, while a reasonable approximation, highlights the limitations of the standard Newton scheme when confronted with the nonconvex optimization landscape inherent to the problem.

Table 1 presents a detailed analysis of the impact of the number of basis functions,  $m_p$ , used in the correction step on the final solution accuracy. A total of 35,752 data points were systematically selected for the subproblems of perturbation expansion. With  $m_p = 600$  basis functions, the relative error was reduced by five orders of magnitude, reaching the scale of  $10^{-12}$ .

Fig. 3a compares the pointwise error of the initialization-step solution  $u_{\text{exact}} - u_N$  with the computed perturbation correction  $u_p$ . The close match between these two fields confirms that the perturbation subproblem accurately models the residual error from the initialization step. Applying this correction reduces the overall error to the order of  $10^{-12}$  (Fig. 3b).

The convergence history in Fig. 3c further illustrates that the Newton method alone stagnates at a local minimum, whereas the correction step drives the residual norm down by several additional orders of magnitude, with the relative  $L^2$  error decreasing proportionally.

Table 1: Convergence analysis for the correction step perturbation subproblem in Example 1. The initialization step employs LRaNN with  $m = 100$  neurons. The perturbation  $u_p$  is constructed from  $m_p$  sinusoidal basis functions using 35,752 sample points.

$m_p$	$error_{L^2}$	$error_{L^\infty}$	Iterations	Residual Norm
100	$1.8883 \times 10^{-7}$	$1.7972 \times 10^{-7}$	3	$1.179 \times 10^{-5}$
200	$4.5914 \times 10^{-8}$	$7.6038 \times 10^{-8}$	3	$6.740 \times 10^{-6}$
400	$2.3975 \times 10^{-10}$	$5.3030 \times 10^{-10}$	3	$1.953 \times 10^{-8}$
600	$2.9075 \times 10^{-12}$	$3.6458 \times 10^{-12}$	6	$1.521 \times 10^{-11}$
800	$2.9045 \times 10^{-12}$	$3.6031 \times 10^{-12}$	6	$1.393 \times 10^{-11}$

Finally, Fig. 3d shows the error trace along the interface  $\Gamma$ , where the perturbation correction almost exactly cancels the initialization-step error, demonstrating highly effective interface recovery.

### 5.2. Example 2

In the second example, we consider a homogeneous nonlinear multi-material interface problem with four subdomains. The computational domain is  $\Omega = [-1, 1] \times [-1, 1]$ , and the coordinate axes  $x = 0$  and  $y = 0$  define the material interfaces, partitioning  $\Omega$  into four quadrants:

$$\Omega_1 = [-1, 0] \times [0, 1], \quad \Omega_2 = [0, 1] \times [0, 1], \quad \Omega_3 = [-1, 0] \times [-1, 0], \quad \Omega_4 = [0, 1] \times [-1, 0].$$

The nonlinear diffusion coefficients in each subdomain are given by

$$\beta_1 = 1 + u, \quad \beta_2 = 1 + 0.5u^2, \quad \beta_3 = 1 + 0.25u^2, \quad \beta_4 = 1 + 0.1u^3.$$

The source terms and homogeneous jump data are chosen so that the exact solution satisfies

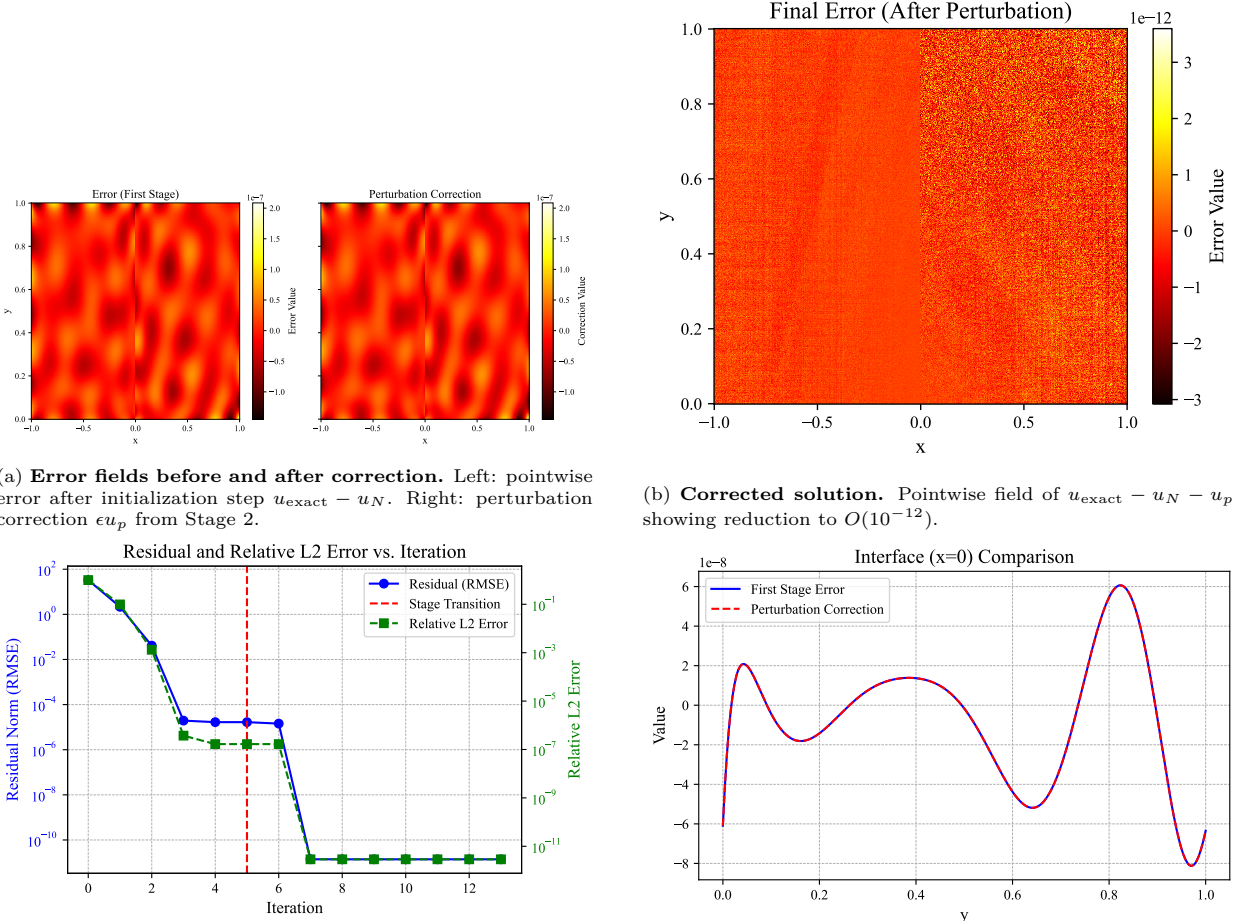
$$u(x, y) = \begin{cases} x^2y^2, & (x, y) \in \Omega_1, \\ e^{-x}x^2y^2, & (x, y) \in \Omega_2, \\ e^{-y}x^2y^2, & (x, y) \in \Omega_3, \\ e^{-(x+y)}x^2y^2, & (x, y) \in \Omega_4. \end{cases}$$

We use local randomized neural networks (LRaNNs) to approximate the solution in the initialization step, applying Newton iteration until the residual norm stagnates. The initialization-step solution  $u_N^\pm$  captures most of the smooth field but, due to the problem's nonconvex optimization landscape, leaves a structured interface residual.

In correction step, we solve the perturbation subproblem using a set of sine basis functions. The computed  $u_p^\pm$  accurately matches the initialization-step error, yielding corrected errors of  $O(10^{-12})$ .

Fig. 4 shows the close match between errors in the initialization step and the computed  $\epsilon u_p$ , as well as the final errors of corrected solution. Interface traces demonstrate excellent cancellation of the initialization-step residual.

Table 2 presents the relative  $L^2$  and  $L^\infty$  errors for the numerical solutions in four subdomains of the computational domain  $\Omega = [-1, 1] \times [-1, 1]$ . The initialization step solution corresponds to the results from the primary Gauss-Newton iterations based on LRaNNs, while the perturbation step solution incorporates an asymptotic perturbation correction with  $\epsilon = 10^{-4}$  to refine accuracy. The perturbation step achieves a remarkable reduction in errors, approaching machine precision across all subdomains, thereby underscoring the robustness and efficiency of the proposed methodology for solving quasi-linear elliptic interface problems with discontinuous coefficients.



(c) **Iteration history.** Residual norms  $\|\mathcal{F}(\alpha^{\{k\}})\|_{l^2}$  and relative  $L^2$  error per Newton iteration. Stage 2 escapes stagnation of Stage 1.

Figure 3: **Example 1: Two-stage optimization results.** Comparison of initialization-step and perturbation-step performance in terms of error reduction, residual decay, and interface accuracy.

### 5.3. Example 3

In this example, we consider a nonlinear elliptic interface problem with complex interface curve and highly nonlinear coefficients. The computational domain is  $\Omega = [-1, 1] \times [-1, 1]$ . The interface  $\Gamma$  is given in polar coordinates  $(r, \theta)$  by

$$r(\theta) = R_0 + A_{\text{plum}} \cos(m_{\text{petal}}\theta),$$

where  $m_{\text{petal}}$  controls the number of lobes, and  $R_0, A_{\text{plum}}$  are constants (see Table 3 for parameter settings). The interface divides  $\Omega$  into the interior  $\Omega^-$  and the exterior  $\Omega^+$ .

The nonlinear diffusion coefficient is

$$\beta(x, u) = \begin{cases} x^2 + y^2 + \exp\left(\frac{1}{2}u\right), & (x, y) \in \Omega^+, \\ 1 + \sin(u), & (x, y) \in \Omega^-, \end{cases}$$

We use local randomized neural networks (LRaNNs)  $u_N^\pm$  to independently approximate the interior and exterior solutions, each with  $m = 500$  neurons and tanh activation. Weights are drawn uniformly from  $[-1, 1]$  and biases from  $[-0.1, 0.1]$ . Newton iteration is applied until the residual norms cease to decay. The

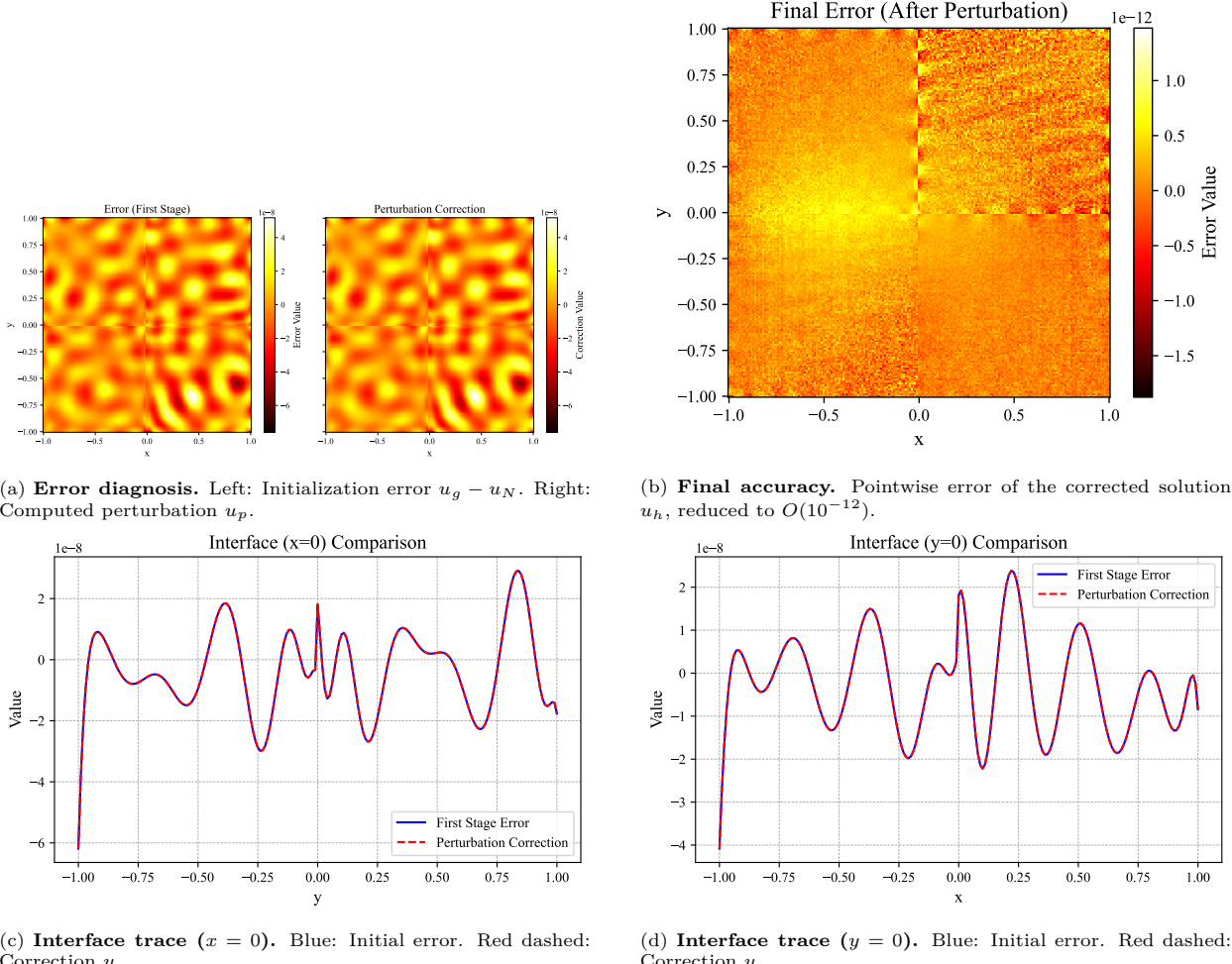


Figure 4: **Example 2 Results.** The correction step effectively eliminates the structured residuals at the multi-material junction.

perturbation subproblem is then solved using two LRaNNs (one per subdomain) with  $m = 2000$  neurons, sin activation, weights drawn uniformly from  $[-7\pi, 7\pi]$  and biases from  $[-\pi, \pi]$ . This step specifically targets and removes the structured residuals from the initialization step. The computed correction  $\epsilon u_p^\pm$  closely reproduces the initialization-step pointwise error, enabling effective cancellation in the corrected solution  $u_N + \epsilon u_p$ . Relative  $L^2$  and  $L^\infty$  errors decrease by roughly 4–5 orders of magnitude. Fig. 5 and Table 3 together demonstrate the effectiveness of the proposed two-step strategy of this case.

Numerical values in Table 3 confirm that, for several  $m_{\text{petal}}$  values, the correction step consistently reduces both  $L^2$  and  $L^\infty$  errors to the  $10^{-8}$  level.

#### 5.4. Example 4

In this example, we consider a high-contrast elliptic interface problem characterized by a large constant diffusion coefficient  $\beta^+ \gg 1$  in the subdomain  $\Omega^+$  and a nonlinear diffusion law  $\beta^-(u)$  in the subdomain  $\Omega^-$ . The problem is posed on the square domain  $\Omega = [-1, 1] \times [-1, 1]$  with a circular interface

$$\Gamma = \{(x, y) \mid x^2 + y^2 = 1/4\},$$

which partitions  $\Omega$  into the inner disk  $\Omega^- = \{x^2 + y^2 < 1/4\}$  and the outer subdomain  $\Omega^+ = \Omega \setminus \overline{\Omega^-}$ . In  $\Omega^+$  we assign a linear diffusion with large constant conductivity  $\beta^+/\beta^- \gg 1$ , while in  $\Omega^-$  we consider a

Table 2: Error comparison for the four-subdomain problem (Example 2).

Subdomain	Initialization step		Correction step	
	$error_{L^2}$	$error_{L^\infty}$	$error_{L^2}$	$error_{L^\infty}$
$\Omega_1$	$4.5790 \times 10^{-8}$	$5.5010 \times 10^{-8}$	$8.6359 \times 10^{-13}$	$8.8042 \times 10^{-13}$
$\Omega_2$	$1.8043 \times 10^{-7}$	$8.5307 \times 10^{-8}$	$1.4879 \times 10^{-12}$	$1.1835 \times 10^{-12}$
$\Omega_3$	$1.2109 \times 10^{-7}$	$6.3436 \times 10^{-8}$	$1.5871 \times 10^{-12}$	$1.0106 \times 10^{-12}$
$\Omega_4$	$2.3272 \times 10^{-7}$	$3.1417 \times 10^{-8}$	$4.6773 \times 10^{-12}$	$1.6778 \times 10^{-12}$

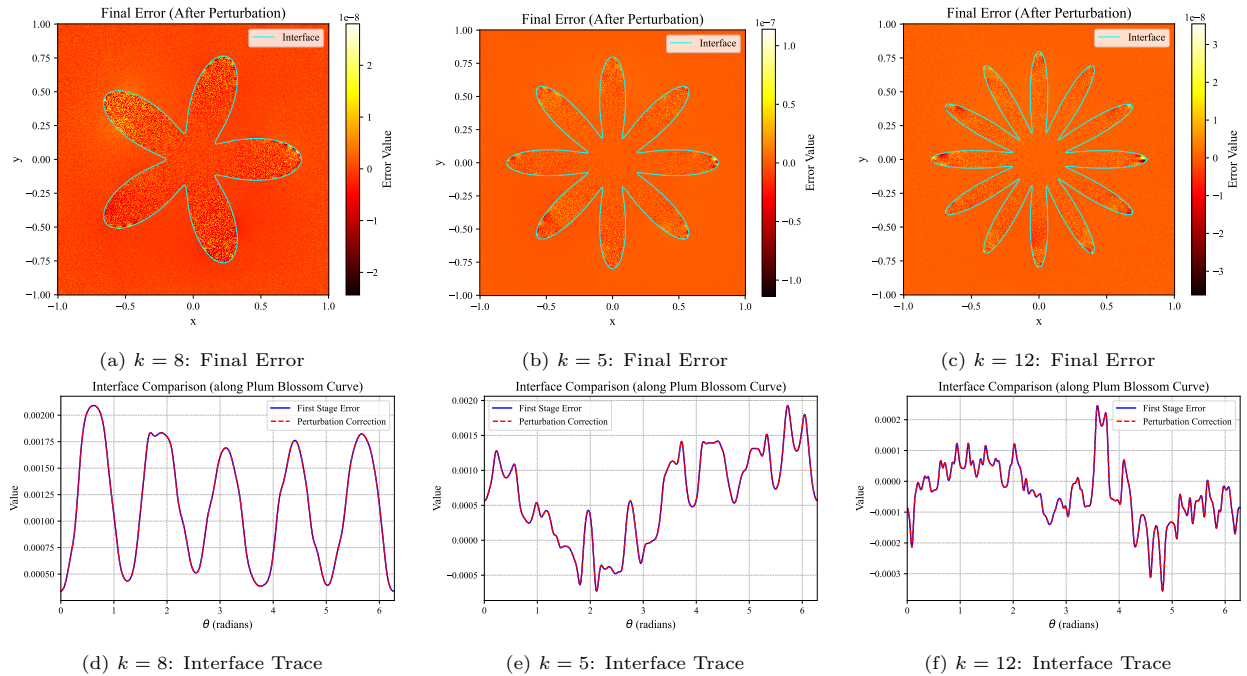


Figure 5: **Example 3 Results.** Performance on complex "plum-blossom" interfaces. Upper row: final pointwise error maps. Lower row: Error along the interface  $\Gamma$  (blue) vs. the computed correction (red dashed).

nonlinear diffusion of the form

$$\beta^-(u) = 1 + u^3.$$

This configuration yields a strong diffusion contrast  $\beta^+/\beta^- \gg 1$  across  $\Gamma$  and introduces additional difficulty through the nonlinearity inside the interface.

The source terms and interface conditions are chosen so that the exact solution is:

$$u(x, y) = \begin{cases} \frac{x^3 + y^3}{\beta^+}, & (x, y) \in \Omega^+, \\ \sin(\pi x) \sin(\pi y), & (x, y) \in \Omega^-. \end{cases}$$

We utilize the same two-step solution procedure as in previous examples: initialization step computes a Newton-based approximation using local randomized neural networks on the two subdomains, while correction step solves the perturbation subproblem to overcome stagnation due to the challenging high-contrast nonconvex landscape.

Fig. 6 presents the main numerical results for this example of case  $\beta^+ = 10^8$ . Fig. 6 compares the pointwise error from initialization step with the computed perturbation correction. Specifically, after the convergence of the first step of Newton's iteration, the relative  $L^2$  norm of the error is  $2.3195e - 06$ , and

Table 3: Quantitative Error Analysis for the Plum Blossom Curve

$m_{\text{petal}}$	Initialization step Solution		Perturbation step Solution	
	$error_{L^2}$	$error_{L^\infty}$	$error_{L^2}$	$error_{L^\infty}$
8	$1.9276 \times 10^{-3}$	$2.0020 \times 10^{-3}$	$2.2966 \times 10^{-8}$	$8.5546 \times 10^{-8}$
5	$2.0911 \times 10^{-3}$	$2.6182 \times 10^{-3}$	$9.9455 \times 10^{-9}$	$3.8079 \times 10^{-8}$
12	$5.1525 \times 10^{-4}$	$2.7786 \times 10^{-4}$	$1.3272 \times 10^{-8}$	$3.9900 \times 10^{-8}$

the relative maximum absolute norm is  $2.3306e - 06$ . The close match between these two fields shows that the perturbation subproblem effectively captures the error of the initial Newton step. Fig. 6b shows the final error after applying the correction, where the residual is greatly reduced across the domain. The relative  $L^2$  norm of the error after perturbation solution is  $9.5015e - 10$  and the relative maximum absolute norm is  $6.6384e - 09$ . Fig. 6c illustrates how both the residual norm and relative  $L^2$  error stagnate in the initialization step, but decrease further in correction step. Fig. 6d also compares the error profile along the interface  $x^2 + y^2 = 0.25$ ; here, the initialization step error and the perturbation are nearly identical, confirming accurate correction of interface-local errors.

 Table 4: Errors of the two-stage method for Example 3 under various diffusion contrast ratios ( $\beta^+/\beta^-$ ).

$\beta^+/\beta^-$	Initialization step		Perturbation step	
	$error_{L^2}$	$error_{L^\infty}$	$error_{L^2}$	$error_{L^\infty}$
$10^4$	$5.04 \times 10^{-8}$	$6.57 \times 10^{-8}$	$1.20 \times 10^{-11}$	$3.11 \times 10^{-11}$
$10^6$	$5.04 \times 10^{-8}$	$6.57 \times 10^{-8}$	$5.23 \times 10^{-11}$	$5.92 \times 10^{-11}$
$10^8$	$2.32 \times 10^{-6}$	$2.33 \times 10^{-6}$	$5.76 \times 10^{-10}$	$2.55 \times 10^{-9}$
$10^{10}$	$2.20 \times 10^{-5}$	$1.65 \times 10^{-5}$	$7.48 \times 10^{-8}$	$2.43 \times 10^{-7}$
$10^{11}$	$2.20 \times 10^{-5}$	$1.65 \times 10^{-5}$	$8.11 \times 10^{-7}$	$2.97 \times 10^{-6}$

Table 4 reports the accuracy of the two-stage method for Example 3 tested under a range of high-contrast ratios ( $\beta^+/\beta^-$ ) from  $10^4$  to  $10^{11}$ ), representing increasingly challenging interface problems. For moderate contrast, the initialization step neural interface solver already yields high accuracy, and the correction step correction further improves all error measures by several orders of magnitude. As the contrast increases, both initial and corrected errors rise, reflecting the intrinsic difficulty of the problem; nevertheless, the two-stage approach enables highly accurate solutions even for extreme contrasts. These results confirm the robustness and effectiveness of our method for high-contrast interface scenarios.

### 5.5. Example 5

In this example, we consider a nonlinear parabolic interface problem with a time-evolving interface  $\Gamma(t)$  separating two materials with distinct nonlinear diffusion laws: the subdomain  $\Omega^+(t)$  has a polynomial-type nonlinearity  $\beta^+(u) = 1 + u^2$ , while the subdomain  $\Omega^-(t)$  exhibits a non-polynomial, exponential-type nonlinearity  $\beta^-(u) = e^u + 1$ .

$$\begin{cases} u_t^+ - \nabla \cdot (\beta^+(x, u^+) \nabla u^+) = f^+(x, u^+), & (x, t) \in \Omega^+ \times [0, T], \\ u_t^- - \nabla \cdot (\beta^-(x, u^-) \nabla u^-) = f^-(x, u^-), & (x, t) \in \Omega^- \times [0, T], \\ \llbracket u(x) \rrbracket = w(x), & x \in \Gamma(t), \\ \llbracket \beta(x, u) \frac{\partial u}{\partial \mathbf{n}} \rrbracket = v(x), & x \in \Gamma(t), \\ u = g(x, t), & (x, t) \in \partial\Omega \times [0, T]. \end{cases}$$

The moving interface is given by

$$\Gamma(t) = \left\{ (x, y) \mid \sqrt{x^2 + y^2} = r(t), r(t) = 0.5t + 0.5 \right\}.$$

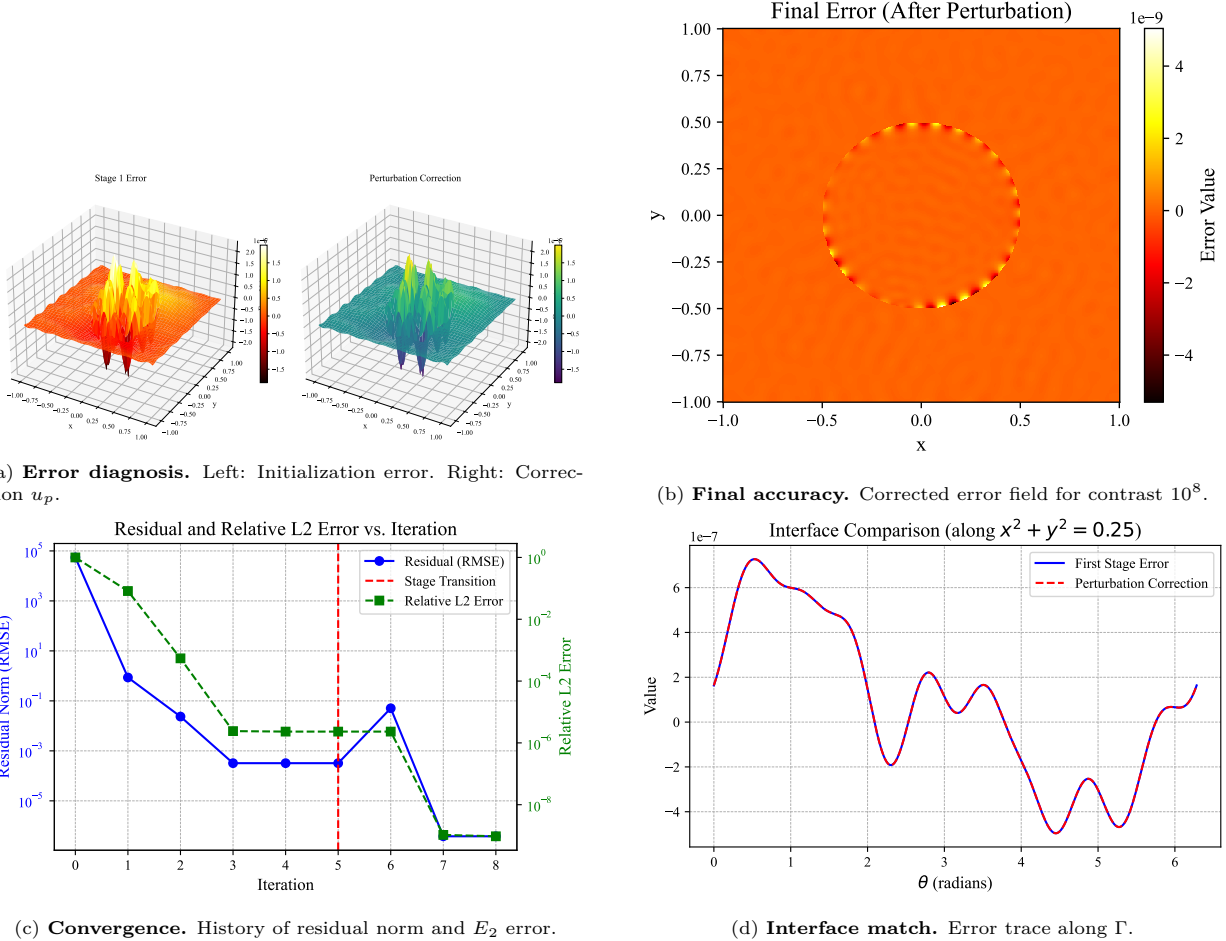


Figure 6: **Example 4 Results.** Robustness under high contrast ( $\beta^+ = 10^8$ ). The correction step recovers accuracy lost due to the ill-conditioned landscape.

We appropriately choose  $f^\pm(x, u)$  so that the exact solution is given as

$$u = \begin{cases} e^{-t} \sin(\pi x) \sin(\pi y), & (x, t) \in \Omega^+ \times [0, T], \\ t(x^2 + y^2), & (x, t) \in \Omega^- \times [0, T]. \end{cases}$$

We solve this problem for  $t \in [0, 0.2]$  in the space-time domain, applying the same two-step framework as in the elliptic cases. In the initialization step for this time-dependent nonlinear parabolic interface problem with a time-dependent interface  $\Gamma(t)$ , the network approximations in the two subdomains are represented by

$$u_N^\pm(x, y, t) = \sum_{j=1}^m \alpha_j^\pm \tanh(w_j^{(1)}x + w_j^{(2)}y + w_j^{(3)}t + b_j),$$

where the weights  $\{w_j^{(k)}\}$  and biases  $\{b_j\}$  parameterize the fixed hidden layer, and  $\{\alpha_j^\pm\}$  are the trainable output coefficients obtained by minimizing the empirical interface-PDE loss.

In the perturbation (correction) step, we seek a refined approximation of the form

$$u_h^\pm(x, y, t) = u_N^\pm(x, y, t) + \epsilon u_p^\pm(x, y, t), \quad u_p^\pm(x, y, t) = \sum_{j=1}^{m_p} \gamma_j^\pm \sin(w_{j,p}^{(1)}x + w_{j,p}^{(2)}y + w_{j,p}^{(3)}t + b_{jp}),$$

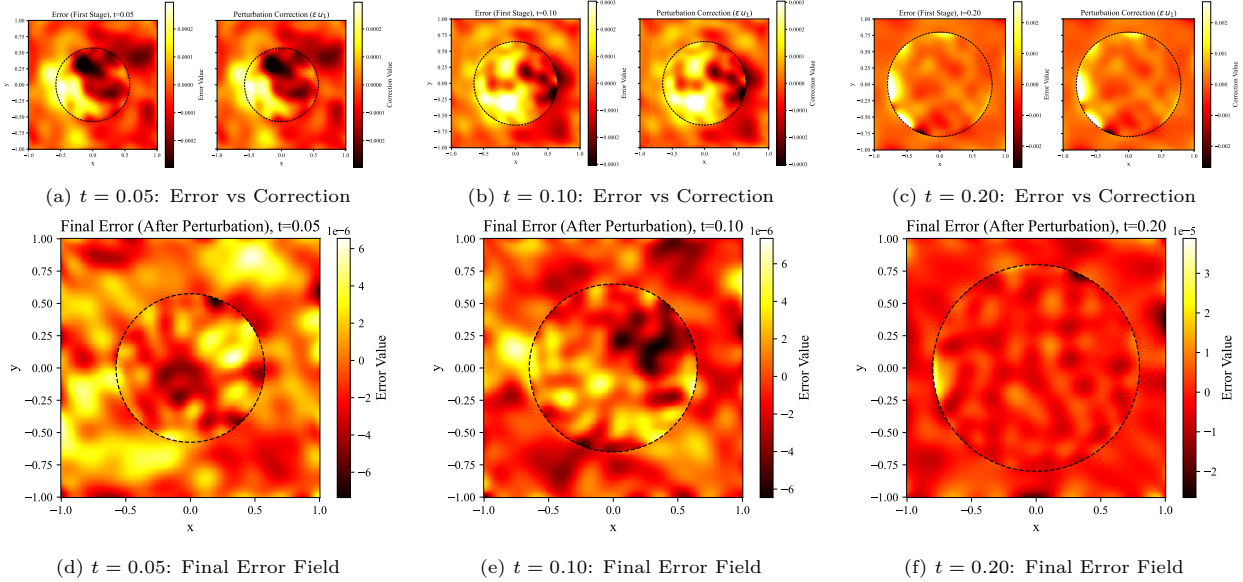


Figure 7: **Example 5 Results.** Space-time error evolution. The correction step (initialized with random space-time features) accurately tracks and eliminates the error propagating along the moving interface.

with independent random features  $\{w_{j,p}^k, b_{j,p}\}$  fixed throughout the correction step, and amplitudes  $\{\gamma_j^\pm\}$  determined by solving the convex quadratic subproblem arising from the truncated second-order Taylor expansion of the continuous objective functional  $G$  about  $u_N^\pm$ .

This construction is a natural space-time generalization of the two-step perturbation framework previously applied to elliptic interface problems: the initialization stage captures the dominant nonlinear solution structure via a tanh-feature representation, while the perturbation stage supplements it with an independent sinusoidal feature set to resolve the residual error. The analogy with the elliptic setting demonstrates the robustness and versatility of the algorithm, as the same conceptual separation of scales and convex post-processing carries over seamlessly to the unsteady, nonlinear, moving-interface context considered here.

From Fig. 7, subplots (a)–(c) clearly show that at  $t = 0.05$ ,  $t = 0.10$ , and  $t = 0.20$  s, the perturbation field recovers both the spatial pattern and amplitude of the initialization-step error, enabling effective cancellation. Subplots (d)–(f) confirm that the corrected error fields are uniformly reduced to the  $10^{-6}$ – $10^{-5}$  level, with negligible deviation along  $\Gamma(t)$ . Subplots (g)–(i) further illustrate that the interface location error is virtually eliminated after the correction step, confirming the ability of the perturbation component to accurately track and compensate residual discrepancies in both the bulk solution and the evolving interface geometry.

### 5.6. Example 6

In this example, we study a class of quasi-linear elliptic interface problems in which the two subdomains exhibit distinct types of nonlinear diffusion: in  $\Omega^+$  the diffusion coefficient depends nonlinearly on the gradient magnitude  $|\nabla u|$ , while in  $\Omega^-$  it depends nonlinearly on the solution  $u$  itself. Namely,

$$\begin{cases} \beta^+ = 1 + |\nabla u|^2, & (x, y) \in \Omega^+, \\ \beta^- = 1 + u^2, & (x, y) \in \Omega^-. \end{cases}$$

We choose the exact solution

$$\begin{cases} u^+ = 0.5 \sin(\pi x) \sin(\pi y) + 0.25, & (x, y) \in \Omega^+, \\ u^- = 0.25 - (x^2 + y^2), & (x, y) \in \Omega^-. \end{cases}$$

Figure 8 reports the results. Panel a shows the initialization–step error and the perturbation correction: the first–stage maximum pointwise error is approximately  $1.5 \times 10^{-4}$ , and the perturbation field reproduces both the spatial pattern and amplitude within  $10^{-6}$ . Panel b presents the corrected error field, where the maximum pointwise error decreases from  $1.5 \times 10^{-4}$  to about  $6 \times 10^{-9}$ , corresponding to a reduction of more than four orders of magnitude. Panel c depicts the residual norm and relative  $L^2$  error versus iteration: in the first stage these stagnate at approximately  $10^{-3}$  and  $10^{-4}$  respectively, and in the correction step both decrease to about  $10^{-8}$  and  $10^{-9}$  within roughly five iterations. Panel d compares the interface error along  $x^2 + y^2 = 0.25$ : the correction curve overlaps the negative of the first–stage error, and the interface  $L^\infty$  error drops from about  $6 \times 10^{-4}$  to  $10^{-8}$ .

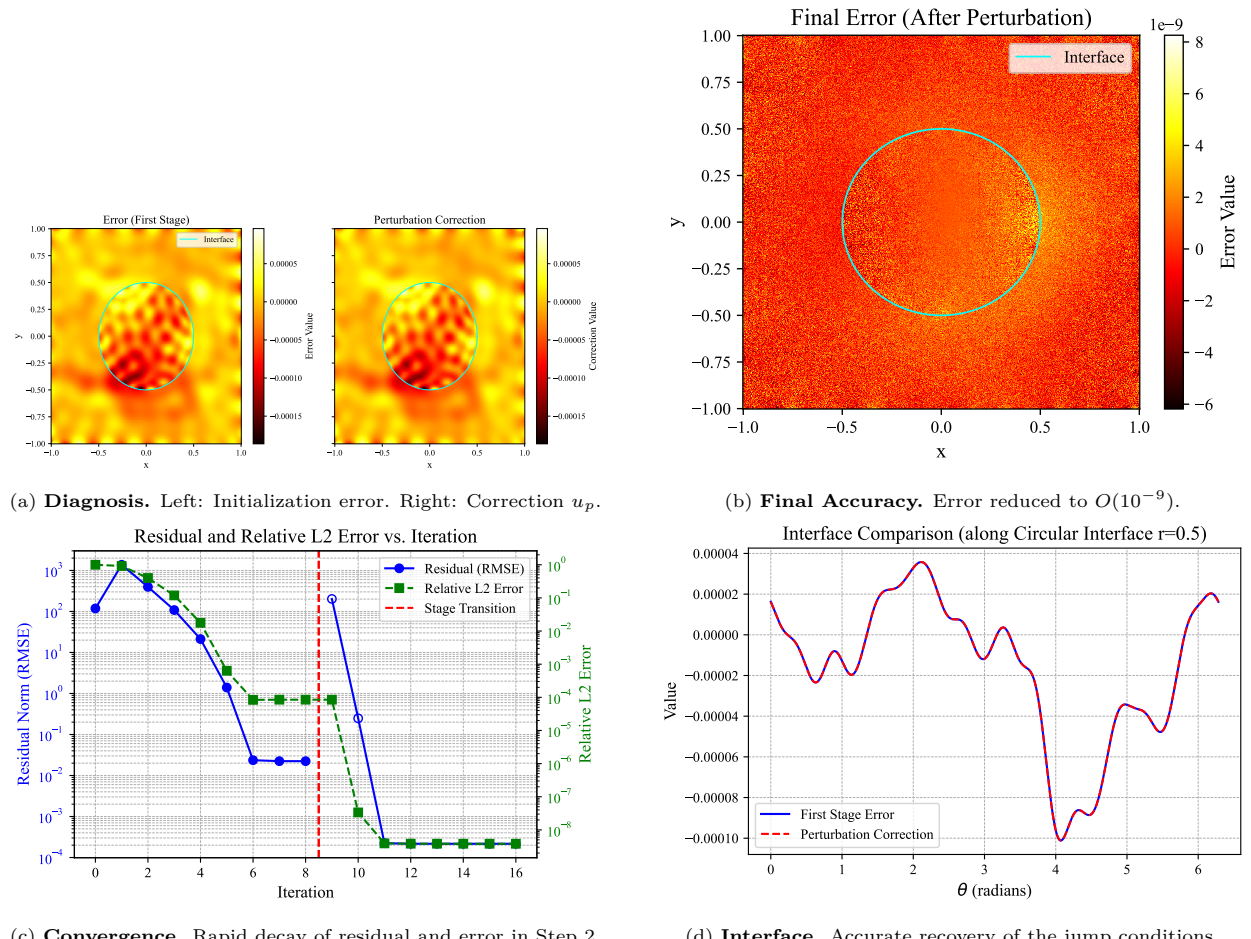


Figure 8: **Example 6 Results.** Performance for gradient-dependent diffusion  $\beta(|\nabla u|^2)$ .

These results verify the robustness of the algorithm for nonlinear elliptic problems with gradient-dependent diffusion.

## 6. Conclusion

In this work, we have developed and validated a robust perturbation-correction method based on LRaNNs for solving quasi-linear elliptic and parabolic interface problems in which the two subdomains follow distinct types of nonlinear diffusion laws, including solution-dependent, gradient-dependent, high-contrast, and time-dependent cases. The proposed method integrates LRaNNs with a Gauss–Newton iteration in the

initialization step to capture the dominant features on the interface and within each subdomain. In the correction step, a perturbation–correction subproblem is derived from a reconstructed equation and solved to reduce the residual error from the initial step. By explicitly targeting the leading error modes from the initialization step, the method achieves an accuracy improvement of about 4 to 6 orders of magnitude, as consistently observed in our numerical experiments.

Extensive numerical tests on problems with static and moving interfaces, complex nonlinear coefficient patterns, and strong contrasts show that the initialization step attains reasonable accuracy but may encounter residual error stagnation, while the correction step consistently reduces these errors by several orders of magnitude, consistent with the error reduction mechanism predicted by our analysis. Moreover, the localized network architecture effectively incorporates the nonlinear interface jump conditions into the optimization objective, handles the interplay between geometric complexity and coefficient discontinuities, and maintains stability without mesh dependency, making the approach applicable to challenging problems for which conventional numerical methods may fail.

The generality and stability of this approach make it applicable to a broad class of nonlinear PDEs whose inherent nonlinearity leads to nonconvex optimization problems. In future work, we aim to extend this perturbation–correction strategy to investigate broader scientific computing domains where high-precision solutions are required despite the presence of a complex nonconvex optimization landscape.

## References

- [1] L. A. Ying, A decomposition theorem for the solutions to the interface problems of quasi–linear elliptic equations, *Acta Mathematica Sinica* 20 (2004) 859–868.
- [2] L. Wang, H. Zheng, X. Lu, L. Shi, A Petrov-Galerkin finite element interface method for interface problems with Bloch-periodic boundary conditions and its application in phononic crystals, *Journal of Computational Physics* 393 (2019) 117–138.
- [3] P. Donato, K. H. Le Nguyen, Homogenization of diffusion problems with a nonlinear interfacial resistance, *Nonlinear Differential Equations and Applications NoDEA* 22 (2015) 1345–1380.
- [4] T. L. Kirk, A. LewisDouglas, D. Howey, C. P. Please, S. J. Chapman, Nonlinear electrochemical impedance spectroscopy for lithium-ion battery model parameterization, *Journal of The Electrochemical Society* 170 (2023) 010514.
- [5] Y. Zeng, P. Albertus, R. Klein, N. Chaturvedi, A. Kojic, M. Z. Bazant, J. Christensen, Efficient conservative numerical schemes for 1D nonlinear spherical diffusion equations with applications in battery modeling, *Journal of The Electrochemical Society* 160 (2013) A1565.
- [6] H. Brenner, *Interfacial transport processes and rheology*, Elsevier, 2013.
- [7] K. E. Teigen, X. Li, J. Lowengrub, F. Wang, A. Voigt, A diffuse-interface approach for modeling transport, diffusion and adsorption/desorption of material quantities on a deformable interface, *Communications in Mathematical Sciences* 4 (2009) 1009.
- [8] S. Wang, A. Nissen, G. Kreiss, Convergence of finite difference methods for the wave equation in two space dimensions, *Mathematics of Computation* 87 (2018) 2737–2763.
- [9] Q. Wang, Z. Zhang, L. Wang, New immersed finite volume element method for elliptic interface problems with non-homogeneous jump conditions, *Journal of Computational Physics* 427 (2021) 110075.
- [10] T. Zhao, K. Ito, Z. Zhang, Semi-decoupling hybrid asymptotic and augmented finite volume method for nonlinear singular interface problems, *Journal of Computational and Applied Mathematics* 396 (2021) 113606.
- [11] Z. Li, K. Ito, *The immersed interface method: numerical solutions of PDEs involving interfaces and irregular domains*, SIAM, 2006.

- [12] R. J. LeVeque, Z. Li, The immersed interface method for elliptic equations with discontinuous coefficients and singular sources, *SIAM Journal on Numerical Analysis* 31 (1994) 1019–1044.
- [13] S. Yu, Y. Zhou, G. Wei, Matched interface and boundary (MIB) method for elliptic problems with sharp-edged interfaces, *Journal of Computational Physics* 224 (2007) 729–756.
- [14] Y. Zhou, S. Zhao, M. Feig, G. Wei, High order matched interface and boundary method for elliptic equations with discontinuous coefficients and singular sources, *Journal of Computational Physics* 213 (2006) 1–30.
- [15] R. P. Fedkiw, T. Aslam, B. Merriman, S. Osher, A non-oscillatory Eulerian approach to interfaces in multimaterial flows (the ghost fluid method), *Journal of Computational Physics* 152 (1999) 457–492.
- [16] X. Liu, R. P. Fedkiw, M. Kang, A boundary condition capturing method for Poisson’s equation on irregular domains, *Journal of Computational Physics* 160 (2000) 151–178.
- [17] I. Babuška, The finite element method for elliptic equations with discontinuous coefficients, *Computing* 5 (1970) 207–213.
- [18] I. Babuška, U. Banerjee, K. Kergrene, Strongly stable generalized finite element method: Application to interface problems, *Computer Methods in Applied Mechanics and Engineering* 327 (2017) 58–92.
- [19] Q. Zhang, I. Babuška, A stable generalized finite element method (SGFEM) of degree two for interface problems, *Computer Methods in Applied Mechanics and Engineering* 363 (2020) 112889.
- [20] T. Lin, Y. Lin, X. Zhang, Partially penalized immersed finite element methods for elliptic interface problems, *SIAM Journal on Numerical Analysis* 53 (2015) 1121–1144.
- [21] P. Hansbo, M. G. Larson, S. Zahedi, A cut finite element method for a Stokes interface problem, *Applied Numerical Mathematics* 85 (2014) 90–114.
- [22] C. S. Peskin, Numerical analysis of blood flow in the heart, *Journal of Computational Physics* 25 (1977) 220–252.
- [23] X. Liu, T. Sideris, Convergence of the ghost fluid method for elliptic equations with interfaces, *Mathematics of Computation* 72 (2003) 1731–1746.
- [24] K. Xia, M. Zhan, G. Wei, MIB Galerkin method for elliptic interface problems, *Journal of Computational and Applied Mathematics* 272 (2014) 195–220.
- [25] M. Kirchhart, S. Gross, A. Reusken, Analysis of an XFEM discretization for Stokes interface problems, *SIAM Journal on Scientific Computing* 38 (2016) A1019–A1043.
- [26] R. Massjung, An unfitted discontinuous Galerkin method applied to elliptic interface problems, *SIAM Journal on Numerical Analysis* 50 (2012) 3134–3162.
- [27] C. Lehrenfeld, A. Reusken, Analysis of a Nitsche XFEM-DG discretization for a class of two-phase mass transport problems, *SIAM Journal on Numerical Analysis* 51 (2013) 958–983.
- [28] M. U. Zapata, R. I. Balam, S. Jerez, An immersed interface method for nonlinear convection-diffusion equations with interfaces, *Partial Differential Equations in Applied Mathematics* (2025) 101250.
- [29] M. Raissi, P. Perdikaris, G. E. Karniadakis, Physics-informed neural networks: A deep learning framework for solving forward and inverse problems involving nonlinear partial differential equations, *Journal of Computational Physics* 378 (2019) 686–707.
- [30] J. Sirignano, K. Spiliopoulos, DGM: A deep learning algorithm for solving partial differential equations, *Journal of Computational Physics* 375 (2018) 1339–1364.

[31] B. Yu, et al., The deep Ritz method: a deep learning-based numerical algorithm for solving variational problems, *Communications in Mathematics and Statistics* 6 (2018) 1–12.

[32] Y. Wang, C. Lai, Multi-stage neural networks: Function approximator of machine precision, *Journal of Computational Physics* 504 (2024) 112865.

[33] Z. Aldirany, R. Cottreau, M. Laforest, S. Prudhomme, Multi-level neural networks for accurate solutions of boundary-value problems, *Computer Methods in Applied Mechanics and Engineering* 419 (2024) 116666.

[34] Y. Pao, G. Park, D. J. Sobajic, Learning and generalization characteristics of the random vector functional-link net, *Neurocomputing* 6 (1994) 163–180.

[35] G. Huang, Q. Zhu, C. Siew, Extreme learning machine: theory and applications, *Neurocomputing* 70 (2006) 489–501.

[36] B. Igelnik, Y. Pao, Stochastic choice of basis functions in adaptive function approximation and the functional-link net, *IEEE transactions on Neural Networks* 6 (1995) 1320–1329.

[37] S. Lin, X. Liu, J. Fang, Z. Xu, Is extreme learning machine feasible? A theoretical assessment (Part ii), *IEEE Transactions on Neural Networks and Learning Systems* 26 (2014) 21–34.

[38] S. Cai, Z. Wang, S. Wang, P. Perdikaris, G. E. Karniadakis, Physics-informed neural networks for heat transfer problems, *Journal of Heat Transfer* 143 (2021) 060801.

[39] J. Chen, X. Chi, Z. Yang, et al., Bridging traditional and machine learning-based algorithms for solving PDEs: the random feature method, *J Mach Learn* 1 (2022) 268–298.

[40] H. Liu, Z. Liu, Q. Xu, J. Yang, Meshfree methods for nonlinear equilibrium radiation diffusion equation with jump coefficient, *Computers & Mathematics with Applications* 147 (2023) 239–258.

[41] Y. Tseng, T. Lin, W. Hu, M. Lai, A cusp-capturing PINN for elliptic interface problems, *Journal of Computational Physics* 491 (2023) 112359.

[42] X. Zhu, X. Hu, P. Sun, Physics-informed neural networks for solving dynamic two-phase interface problems, *SIAM Journal on Scientific Computing* 45 (2023) A2912–A2944.

[43] S. Roy, C. Annavarapu, P. Roy, A. K. Sarma, Adaptive interface-PINNs (AdaI-PINNs): An efficient physics-informed neural networks framework for interface problems, *arXiv preprint arXiv:2406.04626* (2024).

[44] M. Lai, Y. Song, X. Yuan, H. Yue, T. Zeng, The hard-constraint PINNs for interface optimal control problems, *SIAM Journal on Scientific Computing* 47 (2025) C601–C629.

[45] A. K. Sarma, S. Roy, C. Annavarapu, P. Roy, S. Jagannathan, Interface PINNs (I-PINNs): A physics-informed neural networks framework for interface problems, *Computer Methods in Applied Mechanics and Engineering* 429 (2024) 117135.

[46] S. Zeng, Y. Liang, Q. Zhang, High-precision physics-informed extreme learning machines for evolving interface problems, *Engineering Analysis with Boundary Elements* 174 (2025) 106171.

[47] Y. Li, L. Zhang, Physics-informed neural networks for enhanced interface preservation in lattice Boltzmann Multiphase Simulations, *arXiv preprint arXiv:2504.10539* (2025).

[48] F. Ren, P. Zhuang, X. Chen, H.-S. Yu, H. Yang, Physics-informed extreme learning machine (PIELM) for Stefan problems, *Computer Methods in Applied Mechanics and Engineering* 441 (2025) 118015.

[49] C. Lee, Y. Lee, B. Ryoo, A nonoverlapping domain decomposition method for extreme learning machines: Elliptic problems, *Computers & Mathematics with Applications* 189 (2025) 109–128.

[50] X. Zhang, Q. He, An immersed interface neural network for elliptic interface problems, *Journal of Computational and Applied Mathematics* 459 (2025) 116372.

[51] Y. Li, F. Wang, Local randomized neural networks with finite difference methods for interface problems, *Journal of Computational Physics* 529 (2025) 113847.

[52] C. Fan, M. A. Ali, Z. Zhang, Decoupling numerical method based on deep neural network for nonlinear degenerate interface problems, *Computer Physics Communications* 303 (2024) 109275.

[53] C. Fan, S. Lang, M. Toseef, Z. Zhang, A hybrid predictor–corrector decoupled method based on operator learning for solving interface problems, *Journal of Nonlinear Science* 36 (2026) 25.

[54] S. Dong, Z. Li, Local extreme learning machines and domain decomposition for solving linear and nonlinear partial differential equations, *Computer Methods in Applied Mechanics and Engineering* 387 (2021) 114129.

[55] L. Lu, X. Meng, Z. Mao, G. E. Karniadakis, DeepXDE: A deep learning library for solving differential equations, *SIAM review* 63 (2021) 208–228.

[56] E. Kharazmi, Z. Zhang, G. E. Karniadakis, hp-VPINNs: Variational physics-informed neural networks with domain decomposition, *Computer Methods in Applied Mechanics and Engineering* 374 (2021) 113547.

[57] S. Mishra, R. Molinaro, Estimates on the generalization error of physics-informed neural networks for approximating a class of inverse problems for pdes, *IMA Journal of Numerical Analysis* 42 (2022) 981–1022.

[58] S. Mishra, R. Molinaro, Estimates on the generalization error of physics-informed neural networks for approximating pdes, *IMA Journal of Numerical Analysis* 43 (2023) 1–43.